Final Report

To the

NASA INSTITUTE FOR ADVANCED CONCEPTS

AN ULTRA HIGH THROUGHPUT X-RAY ASTRONOMY

OBSERVATORY WITH A NEW MISSION ARCHITECTURE

PHASE 1

Grant 07600-12

For the Period 1 October 1999 through 31 May 1999

May 1999

Smithsonian Institution
Astrophysical Observatory
Cambridge, Massachusetts 02138

The Smithsonian Astrophysical Observatory
is a member of the
Harvard-Smithsonian Center for Astrophysics

1 Introduction

We requested an extension to the Phase 1 NIAC grant and were allowed two months. Therefore, this report is not quite the final report; we describe it as the "Pre-Final Report". However, its content does describe nearly all the activities that have taken place since the initiation of the grant. At the end of the extension period we will send an addendum to this document to update the actual final report.

The objectives of this study can be divided into two major categories, definition of the architecture of a very large diameter,long focal length grazing incidence X-ray telescope and definition of the architecture of the entire observatory and mission. The first objective addresses the question of how the telescope relates to the various focal plane detectors that are present. The second question addresses how the various components of the observatory are launched into space and what is the optimum site in space. This is a pivotal question because launches are probably the major cost driver. The two questions are independent to a considerable extent if we assume the validity of the fundamental premise of this study, that the optimum architecture for an ultra high throughput X-ray astronomy observatory is indeed one in which the large telescope and all detectors/spectrometers are on separate spacecraft.

There is a natural way to divide the activities among SAO, MSFC, and LERC. SAO's expertise is in the area of X-ray optics. Also, the PI at SAO is the principal motivating force in this study. Therefore, SAO's engineering studies addressed the telescope. LERC's specialty is propulsion including ion engines. MSFC has general experience in the area of space technology and sending large masses into space. Consequently MSFC could be instrumental in defining the mean of launching the largest, most massive component of the observatory, the telescope.

2 Relevance of the High Throughput X-ray Observatory to NASA's Science Objectives

2.1 Distribution of Matter in the Universe

During the past few years there has been a great effort by theoreticians to understand the evolution of the universe through simulation. For example participants in the Grand Challenge Cosmology Consortium have carried out detailed calculations of how the universe has evolved based upon cosmological models. The process of star formation results in the build up of metals and their release into the intergalactic medium. The consensus conclusion is that most of the baryonic matter exists today at low z as hot intergalactic gas with temperatures ranging from 100,000 to ten million degrees (e.g. Cen and Ostriker, 1998). Stars, galaxies, and clusters of galaxies account for perhaps 20 percent, of all the baryonic matter in the Universe. This is true also for non-baryonic matter which is much larger mass but detectable only indirectly through gravitational effects upon baryonic matter. The gas is highly structured; it consists of filaments as shown in Fig. 1 which appears in Cen and Ostriker, 1998. Simulations suggest that averaging globally the metallicity of the universe increases from 1 percent of the solar value at $z = 3$ to about 20 percent at present (Cen and Ostriker, 1999). Denser regions are predicted to be more metal rich.

Fig 1 (Cen and Ostriker) Density of hot gas at low z.

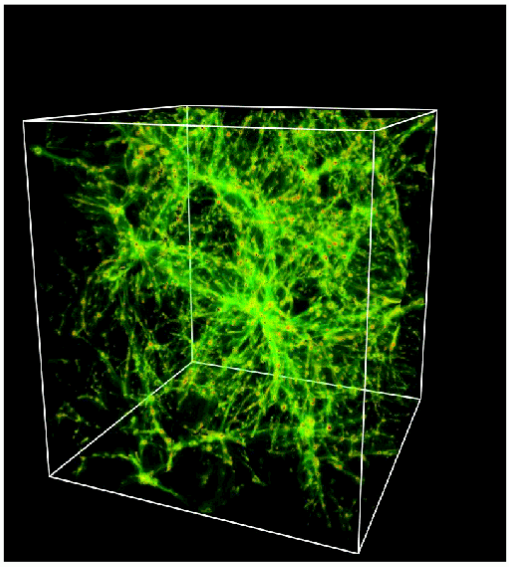

The significance of this finding is that hot gas can be studied only be only in X-rays. Where the gas is dense, for example the intracluster medium of a cluster of galaxies, it can be detected in emission. Where it is less dense it can be detected as resonant absorption lines in the X-ray spectrum of a background quasar. The evolution of its chemical composition from very low to near solar elemental abundance reflects the history of star formation. Observing the emission and the absorption lines in the X-ray band allows us to reconstruct the what is in effect the "structure and evolution of the universe", the research theme that reflects the scientific goals of NASA and the astronomical community.

Research that address directly will accelerate rapidly when the Chandra Observatory is launched in the summer of 1999. According to current plans it will be followed within a year by ESA's XMM, and Japan's ASTRO-E. These missions contain 1m class X-ray telescopes. However, the these missions will eventually be limited to probe deeply by confronted with a shortage of photons. For this reason we are already planning the next generation, higher throughput 3m class telescope missions with an order of magnitude more collecting area. They are the Constellation X-ray Mission of NASA and the XEUS mission of ESA. They represent the best that can be achieved with current technology and current mission architectures. However, they too are likely to come up against the photon limit at a point when much work will still remain to be done.

We estimate that the long term goal should be a **30m telescope** which has an effective area of **2 million sq. cm**.. Our criterion and the details of the estimate are shown in Appendix A. This goal is in accord with other estimates.

2.2 Gravitation Lensing

Gravitational lenses are an increasingly powerful tool in cosmology. As described by Munoz, Kochanek, and Falco, 1999 there are 1, 0.1, and 0.01 gravitationally lensed X-ray sources per square degree with fluxes exceeding 10^{-15}, 10^{-14}, and 10^{-13} ergs/sec. Deep X-ray images of clusters of galaxies should yield one multiply-imaged X-ray source per 3, 30, and 300 clusters. This effect cannot be utilized to advantage in visible light because of the confusion from stars and in radio because of the complex morphology of radio sources. The separation between multiple images is larger than 2.5 arcseconds for only one-tenth of the systems. Hence, the telescope has to have excellent angular resolution to study the lenses effectively. It is an intrinsic property of the grazing incidence geometries of X-ray telescopes that one arcsecond resolution can exist only over a few arcminutes of field. If the resolution is worse we require larger angular separations between quasars which reduces the number of useful lens systems. Therefore, in order to obtain a large number of lensed quasars very many exposures have to made. This places a practical limit on the length of an exposure. Consequently, the X-ray telescope has to have very high throughput as well as very good angular resolution to attain the potential of gravitationally lensed quasars in cosmology.

2.4 X-rays and the Early Universe

The deep field exposures of the Hubble Space Telescope seems to have reached the maximum distance from which visible light can originate (Vogeley, 1998). The fields contain no visible light beyond the resolved objects. The reason is attributed to absorption in a heavy concentration of dust produced by early generations of star formation. However, X-rays above 2 keV can penetrate the dust and possibly reveal the earliest quasars and starburst galaxies. The quasar spectra will have highly redshifted absorption edges from Si, S and Fe that can be detected in a very high throughput system. The strength of the edges is sensitive to only the chemical abundances, and not the size, shape, or condition of the dust grains. Therefore, we can measure chemical abundances in the early universe and the extent to which star formation has occurred.

3 The Architecture of the Observatory

The Phase 1 study began with the following specifications for the ultra high throughput X-ray observatory:

1) > 10 m diameter aperture telescope providing > 2E05 cm{2} of effective area at 2 keV with an angular resolution of several arcseconds or better,

2) focal length of > 100 m,

3) accommodation of unlimited number and large variety of detectors including imagers, spectrometers, polarimeters, etc.

4) replacement of detectors that are exhausted, have failed, or are obsolete,

5) not dependent upon the success of a single launch,

6) long life, at least 15 years,

7) the cost per effective area must be much lower than previously,
and the total cost should not exceed the cost of current large
programs like, for example, the Chandra X-ray Observatory.

As described in the Phase 1 proposal, the standard mission architecture of the Chandra X-ray Observatory, XMM, and ASTRO-E, i.e. the launch of a single spacecraft with a fixed, inaccessible payload, fails to satisfy virtually any of the above. It is difficult for a mission with the conventional architecture, i.e. a single spacecraft containing the telescope, an optical bench, plus all the detectors, to satisfy these requirments. This motivated us to consider a new mission architecture of distributed spacecraft based upon placing the telescope and all detectors upon separate spacecraft with no optical bench to connect them. The optical bench is replaced by station keeping to an accuracy of several millimeters between the telescope and the detector at the focus. The other detectors that are standing by also perform some degree of station keeping to avoid wandering away from the telescope's vicinity. However, their accuracy need be no better than a hundred meters. This concept is shown in Fig. 2.

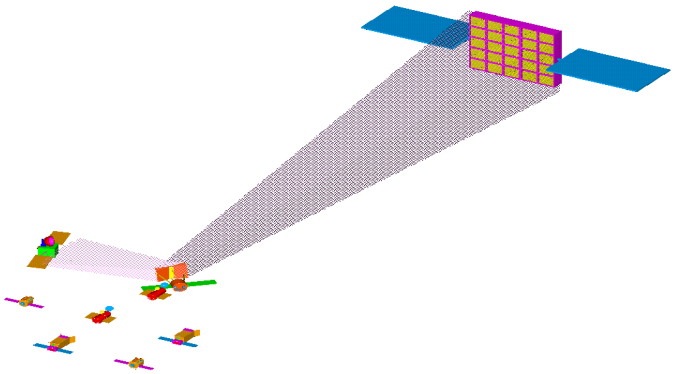

Fig. 2 High Throughput X-ray observatory with telescope and detectors on separate spacecraft.

During the course of the Phase 1 study, following some interchange of ideas at the January AAS meeting in Austin the goal for the size of the telescope increased. The 10 m diameter, 100 m focal length specification was increased to 30m diameter and the focal length in the range 250 to 300 m. This is based upon the requirement that the observatory be able to measure the intensity of an X-ray absorption line with an equivalent width of 0.05 eV in 10E04 seconds with a precision of six sigma. The calculation is shown in Appendix A. The area of the telescope, hence also its mass increased a factor of 10 and its length a factor of three. With the lightest material that is currently used in the fabrication of X-ray telescopes, 5 mil Al foils at the Goddard Space Flight Center, the mass of the telescope would be 30 tons. At this point no matter what novel material of even lower

mass we are able to find for the telescope's substrates its mass will exceed the capabilities of any single launch vehicle.

Increasing the area and focal certainly extinguished any remaining possibility that this observatory could be built with conventional architecture. Furthermore, the increase in focal length to about 300 m made it more difficult for the observatory to operate in low Earth orbit where gravity gradient forces are significant and make station keeping difficult. Constantly overcoming the gravity gradient forces will result in rapid consumption of the spacecraft's propellant which it also uses for attitude control. The alternative is to send the spacecraft to a high orbit. Since X-ray instruments cannot operate between about 15,000 km and 50,000 km because of high radiation background they must be sent higher. The less costly alternative to high orbit, the highly elliptical orbit, e.g. 100,000 km apogree and 10,000 km perigree favored by many missions, is too difficult an environment for station keeping. At this point the best site appears to the Sun-Earth L2 point. This is about one million miles from Earth, on the dark side.

The consequences of siting the observatory well above the Earth are that the telescope is too massive to get there in a single launch. That is, it must be constructed in situ. In this case the construction project requires a high degree of precision because the product is a high resolution telescope. We require an "enabling" technology that does not exist currently, remote or tele-robotic construction projects.

4 The Architecture of the telescope.

4.1 Introduction

The 30m telescope has an effective area of about 2 million square centimeters. This is about 1000 times larger than AXAF/XMM and 100 times larger than the ``Next Generation" Constellation X-ray Mission and XEUS. While this effective area is very large in comparison to any previous or planned X-ray telescope it is no larger than the combined area of the European Southern Observatory's four VLT mirrors. The great challenge is to make the telescope with a much lower mass to area ratio than current telescopes. New materials and new techniques will be required to do so and simultaneously obtain an angular resolution of about an arcsecond.

Deploying such large area at L2 requires a radical change in the design and construction of the telescope and the means of taking it to L2. The telescope will certainly have to be segmented into smaller units, a total of several hundred or so. The only hope of achieving high angular resolution is to provide each segment (or a group of segments) with a positioning system for alignment to a common focus. The segments would be delivered in series over a period of many years and integrated with the others. Since many deliveries will be required, the feasibility of this concept is also dependent upon another "enabling technology", a new method for launching payloads into space at much lower cost per kilogram.

4.2 Grazing Incidence Telescopes

An X-ray telescope reflects rays incident at low angles or grazing incidence. The most familiar type of X-ray optics for astronomy is the double conical telescope, especially the Wolter Type 1

parabola/hyperbola. This geometry has been employed in every X-ray telescope mission to date and in all waiting to be launched. It is certainly a candidate for the Ultra High X-Ray Observatory. It can be made in segments. The Goddard Space Flight Center made double conical telescopes consisting of fixed quadrant segments with aluminum foil reflectors for ASCA and ASTRO-E. ESA is planning to make the 3m XEUS telescope in this geometry with position controllers on the segments (Bavdaz et al, 1999). The XEUS telescope will be relatively heavy because the reflectors are made of nickel, even they are quite thin.

Orthogonal parabolas or the ``Kirkpatrick-Baez" geometry is another option (Fig. 3). The geometry is essentially rectangular and it can be segmented rather easily into segments of equal size and shape (Fig. 4). Internally, the reflector can be segmented along its length for a piecewise linear approximation of a parabola. The result is that this geometry can achieve a theoretical angular resolution of one arcsecond with nearly all the reflectors being simple flats. For a few reflector segments, those furthest from the optic axis, a slight curvature is required to stay under one arcsecond. Small curvature may be applied to a flat by varying the thickness of the heavy metal coating along the length. This technique is being investigated by W. Cash and D. Windt (private communication) for small reflectors. Another possible advantage of the K-B geometry is the apparent ability to unfold a group of segments into a thin pancake for observing from a cylindrical volume that is stowed conveniently in the envelope of the space craft that delivers it to L2. The folded and unfolded array of telescope segments are shown in Fig. 5 and Fig. 6.

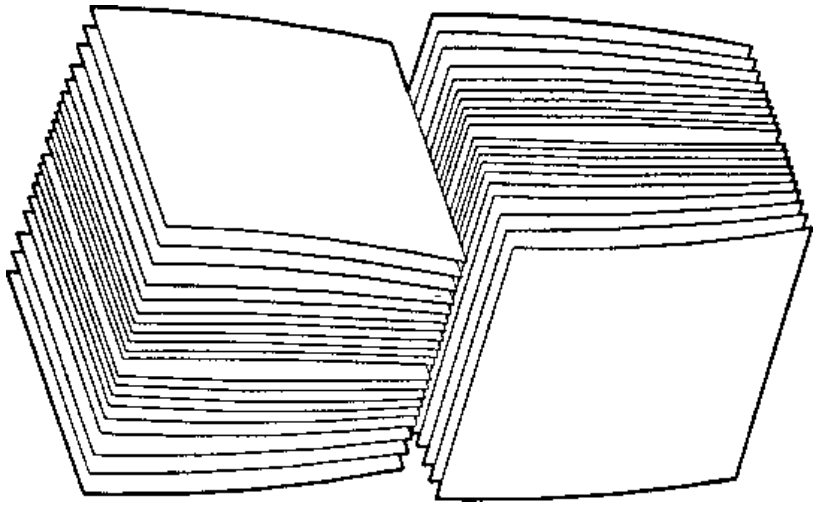

Fig. 3 Kirkpatrick-Baez Telescope, orthogonal 1D parabolas (above)

Fig 4 Segmentation of Kirkpatrick-Baez Telescope into equal size modules (below)

Fig. 5 Folded (bottom left) and Fig. 6 Unfolded array (lower right) of segments

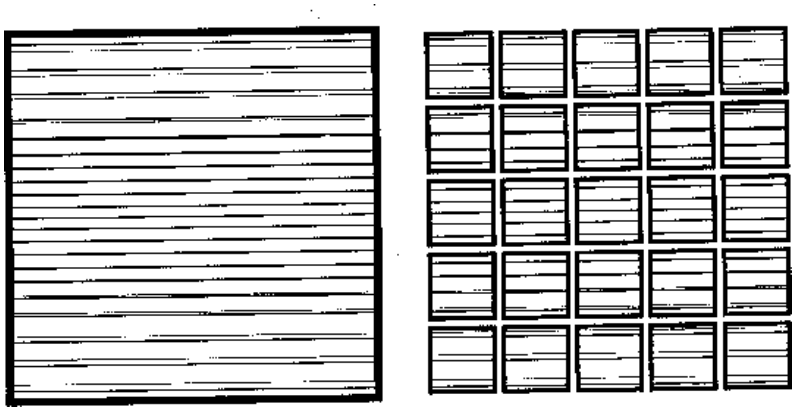

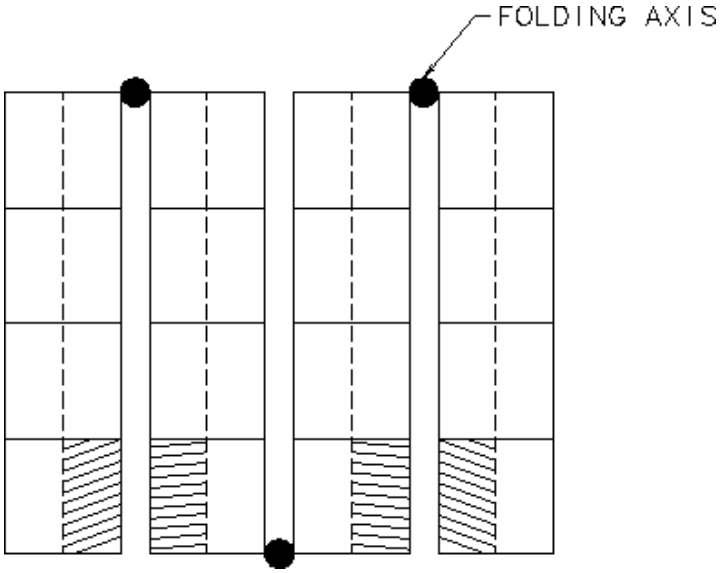

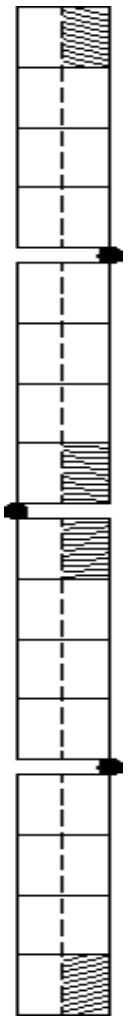

5 Engineering Studies of a Kirkpatrick-Baez X-ray Telescope

During phase 1 an approach to constructing a segmented Kirkpatrick-Baez was the subject of an engineering study. The design is illustrated below in Fig. 7.

Fig 7 Segmentation of K-B mirror, unequal depth of mirror

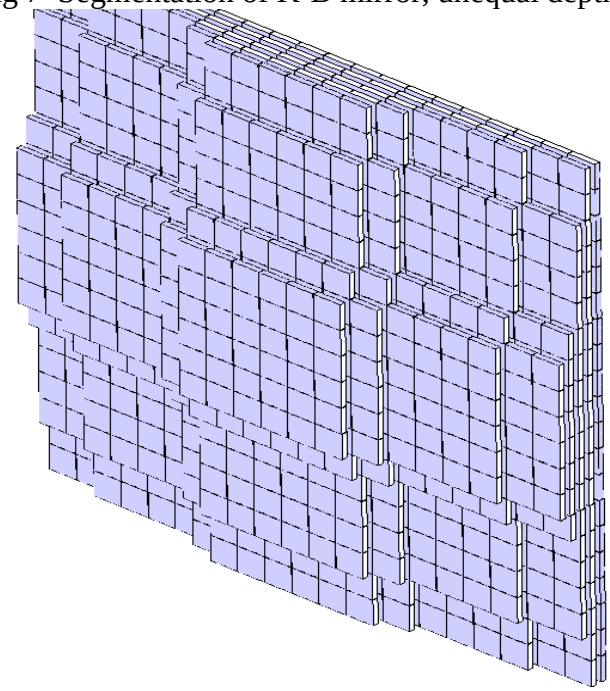

This telescope consists of a large number of segments each containing a single flat reflector. Each reflector is oriented to reflect an incoming beam of parallel rays to a common focus. The flats are located by being forced up again precision spacers. This design has the advantage of concentrating more mass towards the center of the telescope than other designs and therefore has a relatively low moment of inertia. This is described in more detail in Appendix B.

6 Engineering Study of the Reflectors of a Kirkpatrick-Baez Telescope

The mass of the telescope is ultimately determined by the mass of the reflectors. Therefore we seek the least dense material possible. To date the X-ray telescopes with the best ratio of effective area to mass is are the 125 micron thick aluminum foil double conical mirrors made at the Goddard Space Flight Center. The problem with this approach is that its angular resolution is at the level of an arcminute whereas our goal is the arcsecond. This material lacks stiffness so it difficult to imagine an aluminum foil telescope with arcsecond resolution. Seeking a even lighter we turned our attention to plastic film. Plastic film has been considered before in Japan and more recently at SAO by Schnopper and co-workers. Both efforts were double conical mirrors. In our case, the reflectors are flats so it seemed promising to consider plastic film under uniform tension. We carried out an engineering analysis of stretched polyimide film. The analysis is given in Appendix C.

7 Ion Propulsion

Two main propulsion challenges exist for the deployable Ultra-High Throughput Telescope; delivery of the telescope wholly or in pieces to the L2 point with small, affordable launch vehicles, and long term L2 point maintenance and pointing once at the L2 point. (Propulsion is also needed for delivery and maneuvering of the many receiver satellites.) If one propulsion system can perform both missions, perhaps by throttling, all the better. Several candidate technologies are in development which could perform either function. For the delivery, a high Isp, high power electric propulsion device would allow for use of a smaller launch vehicle, especially if the complete 30 MT telescope is to be delivered in one piece. Only the Energia launch vehicle (now mothballed) could possibly place such a large payload at the L2 point using conventional chemical propulsion.

The solution to this problem must be a found by combining transfer orbit design and propulsion system technology. Included in the propulsion system technology selection is the optional use of advanced power collection and storage technologies. The options for delivering the telescope components include:

1. Conventional Chemical performing a large perigee burn at parking orbit to reach the L2 point. (Quickest but lowest payload solution.)
2. High Isp electric propulsion using a nearly continuous thrusting spiral to reach the L2 point. (Requires large power collection systems and the most fuel of the electric propulsion concepts. Long trip times.)
3. High Isp electric propulsion with coast period to create a highly elliptic transfer orbit to the L2 point. (Requires less fuel than option 2 and, in some cases, longer trip times.)
4. High Isp electric propulsion using a store-burn concept to continuously perform perigee burns and raise apogee to reach the L2 point. (Requires the least fuel of the electric propulsion options and a smaller power collection system. Does require a large storage system but can use higher power, higher efficiency electric propulsion devices. In some cases the longest trip time of 2,3, or 4.)
5. Modification of 3. And 4. Add a simple chemical stage (perhaps solid) to complete the mission once the orbit is high enough. (Greatly reduces trip time at the expense of some payload.)

A trade study combining the above mission options with available and planned electric propulsion and power technologies must be performed to find the best combination in terms of performance (mass and trip time) and cost.

The other missions to be performed include L2 stationkeeping and telescope pointing re-pointing and holding. These requirements are fairly well understood based on other platforms which have used the L2 point with success (e.g. SOHO). Control authority and jitter along with the required power levels must be explored. Some electric propulsion devices can create contamination which could coat the telescope with time.

The potential electric propulsion systems for the L2 delivery and on-station control can be catagorized as either electrothermal, electrostatic, or electromagnetic devices. A wide range of power levels for electric propulsion have been developed, both the high and low power have a place on the conceptual telescope. Electrothermal devices include resistojets and arcjets which heat the working fluid resistively or with an arc and expand the fluid or a nozzle. (Lichon, Haag) An arcjet schematic is shown in Figure 8. Such devices are not very high Isp (300 to 600 sec) unless hydrogen propellant is used (~1000 sec). Hydrogen is stored cryogenically at a very low density and would compete for payload shroud space with the payload telescope.

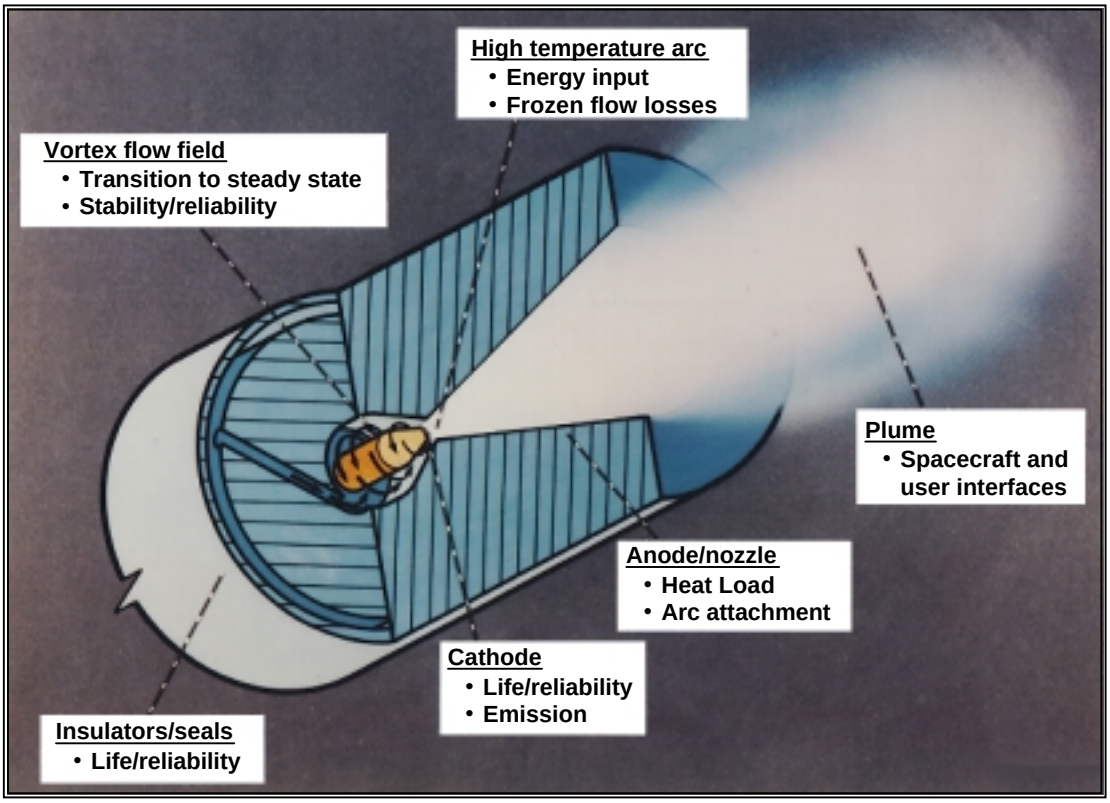

Figure 8 Arcjet Components and Operation

Electrostatic devices exist in two current forms, the Hall thruster and the gridded ion thruster. (Sankovic, Sovey) Both achieve high acceleration rates of the working fluid - usually a heavy noble gas such xenon or krypton - by ionizing the fuel and using a high voltage potential to accelerate the ions. Schematics are shown in Figures 9 and 10. Such devices have been flown in the 500 W to 2.5 kW range with good Isp performance (1500 to 3000 sec) and acceptable lifetimes. The Hall thruster is usually preferred in the 1500 sec to 2500 sec range with the Ion thruster have better performance above this Isp range.

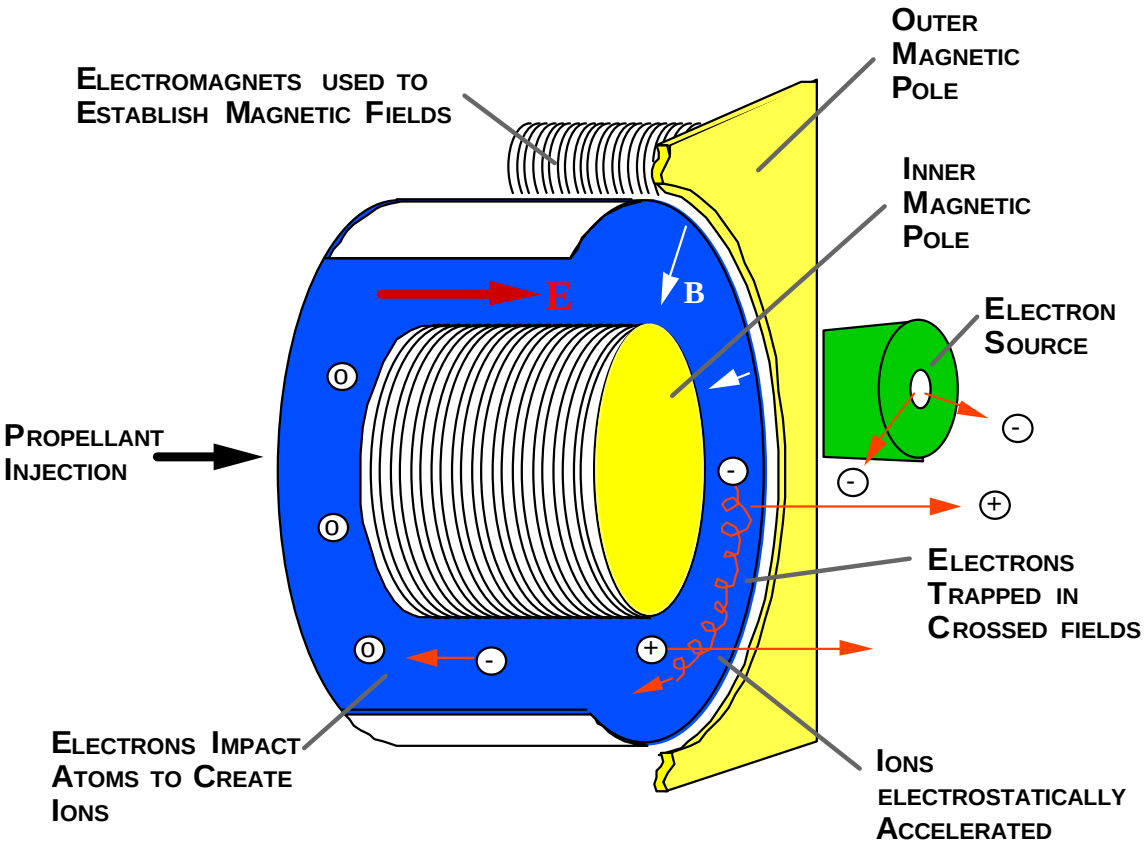

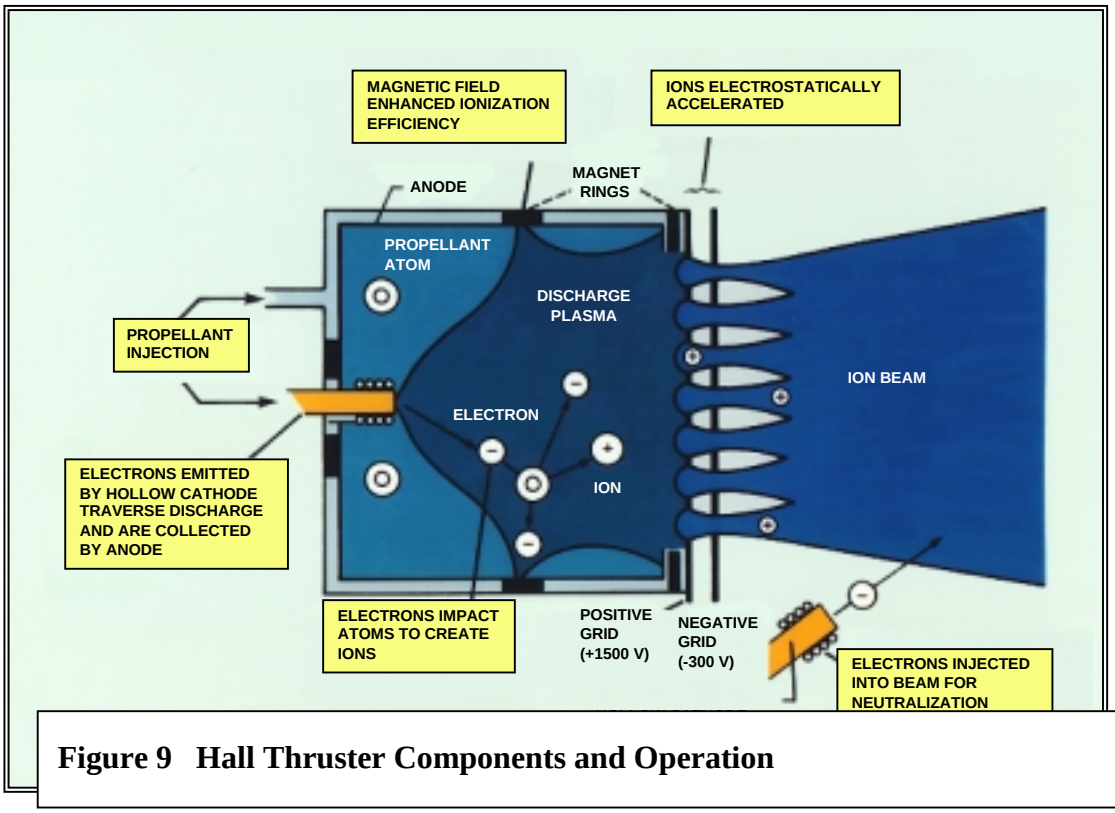

Figure 9 Hall Thruster Components and Operation

Figure 10 Ion Thruster Components and Operation

Finally, magnetoplasmadynamic (MPD) thrusters utilize a magnetic field in some cases self-induced with a high voltage arc, in other cases with an applied field to accelerate ionized fuels to over a wide range of Isps (1000 to 7000 sec) depending on the fuel type. (Myers) An MPD schematic is shown in Figure 11. The simplelist form of an MPD an the only one used operationally to date is the Pulsed Plasma Thruster (PPT). (Blandino) A PPT schematic is shown in Figure 12. Using an arc applied over the face of a teflon fuel bar the PPT accelerates the vaporized teflon with a self-induced field in a pulsed mode using a capacitor storage device. Isps in the range of 1000 sec have been demonstrated. The PPT is perhaps best suited to attitude control and small maneuver responsibilities. Other MPD devices have been flow as experiments and are being actively researched today, especially in the high power region (above 100 kW) where electrostatic devices would be very large.

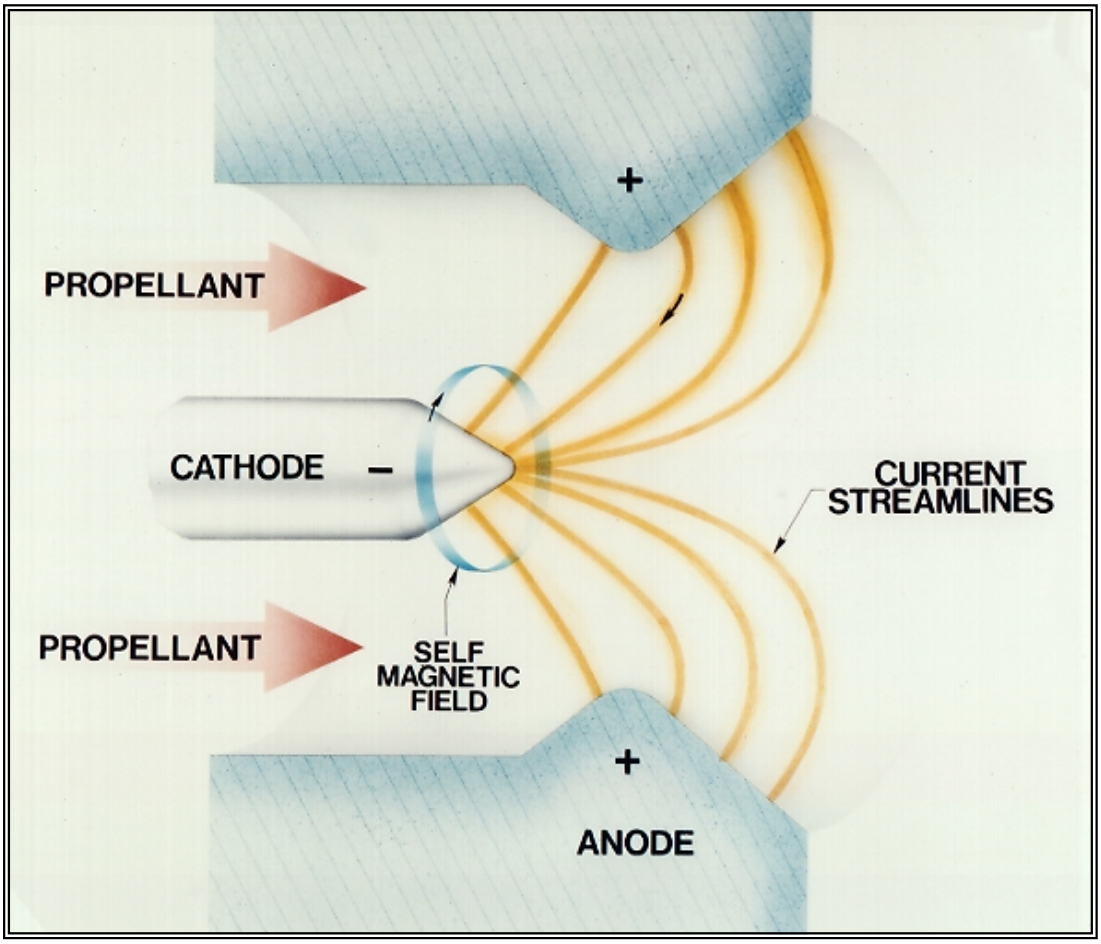

Figure 11 MPD Thruster

Appendix A
Estimate of Number of Photons and Time Required to Measure the "X-ray Forest" Absorption Lines in the Spectrum of a Quasar

These estimates will be used in the NIAC Phase 2 proposal to justify ultra high throughput

From information given in Hellsten et al paper on the X-ray forest estimate the time required to
detect weak absorption lines at ~ 0.5 keV in the spectrum of a quasar

(Schwartz and Tucker, 1988)

$$NQ(E) := \left(100 \cdot E^{-1.7 + 0.26 \cdot \log(E)}\right) \cdot \exp\left(\frac{-E}{125}\right)$$ **relative number of photons per sec-cm^2-keV**

$NQ(1) = 99.203$
$NQ(10) = 3.352$
$NQ(100) = 0.196$
$NQ(300) = 0.022$
$NQ(600) = 1.582 10^{-3}$

Photon Spectrum

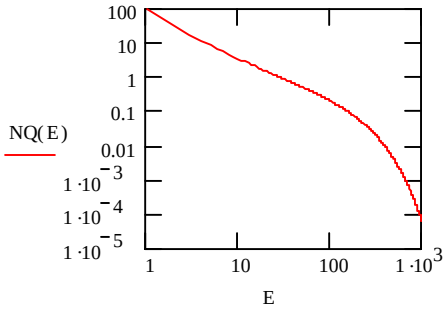

$EENQ(E) := E^2 \cdot NQ(E)$

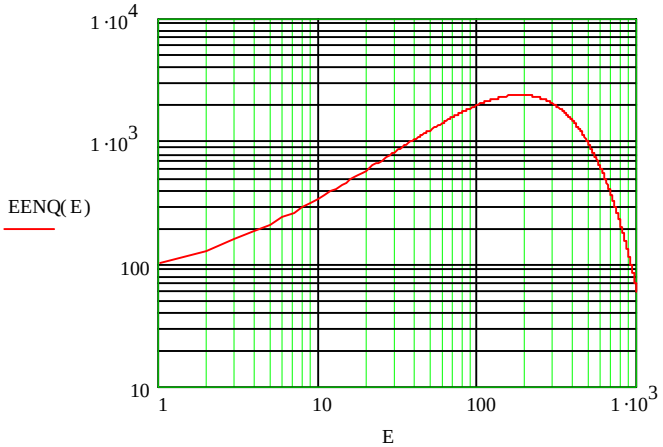

Relative Energy Flux per Decade
Normalize the 0.5-2 keV energy flux to F, in ergs/sec-cm2

$F := 10^{-13}$

$$Norm := \int_{0.5}^{2} E \cdot NQ(E)\, dE$$

Norm = 140.928 **keV** **ergs/s-cm^2 (0.5-2 keV)**

$NormErgs := Norm \cdot 1.6 \cdot 10^{-9}$ $NormErgs = 2.255 10^{-7}$

$$B := \frac{F}{NormErgs}$$ $B = 4.435 10^{-7}$

Normalization factor of spectral function

$$EnFlux := B \cdot \int_{0.5}^{2} E \cdot NQ(E)\, dE$$

$EnFlux = 6.25 \cdot 10^{-5}$

$EnFluxErgs := EnFlux \cdot 1.6 \cdot 10^{-9}$ $EnFluxErgs = 1 \cdot 10^{-13}$ **OK**

$Intensity := EnFluxErgs$

Calculate the photon flux/sec-cm^2-keV at 0.5 keV and the flux in 2 eV bin

$Res := 2$ **eV** $Intensity = 1 \cdot 10^{-13}$ **ergs/sec-cm^2 0.5-2 keV**
$Photon\_Flux := B \cdot NQ(0.5)$

$Photon\_Flux = 1.515 10^{-4}$

$Photons\_bin\_sec := Photon\_Flux \cdot Res \cdot 10^{-3}$ $Photons\_bin\_sec = 3.03 \cdot 10^{-7}$

$Sigma := 6$ $Res = 2$ **eV** $Weq := 5 \cdot 10^{-2}$ **eV** $Time := 1 \cdot 10^{5}$ **sec**

$$N\_Continuum := Sigma^2 \cdot \left(\frac{Weq}{Res}\right)^{-2}$$

Number of photons in continuum with in bin of width Res

$N\_Continuum = 5.76 \cdot 10^{4}$ $$Area := \frac{N\_Continuum}{Photons\_bin\_sec \cdot Time}$$

$Area = 1.901 \cdot 10^{6}$ **cm^2**

Appendix B UHTT Mirror Array Layouts

The UHHT Array is a Kirkpatrick-Baez system, which consists of two orthogonal sets of mirrors. The first set would focus the incoming rays into a line, the width of the array, if the second set didn't exist. The second set takes the reflected rays from the first, and completes the focusing in the orthogonal direction.

The array is composed of mirror sections that are sufficiently narrow in the optical axis direction, so that many flat mirrors can approximate the parabolic shape to meet the optical requirements. There are two ways that the flat sections might be arranged, a single row of mirrors, like a venetian blind, or sets of mirrors arranged front-to-back to form deeper sets of parabolas, with wider spacing between them. The first requires shallower frames, which may offer weight savings, but the second has less obscuration, since the edges of the back mirrors can be shadowed by the mirrors in front, and only the edges of the forward-most mirrors block incoming rays.

The geometry is such that the mirrors closer to the optical axis have a shallower grazing angle than the outer mirrors, and need to be closer together in order to fully fill the aperture. At some point, the spacing becomes impractical, and the mirrors have to be placed behind each other. At the center of the array, far too many mirrors would be required, and the aperture would be masked in that area, which might be used for structural members, electronics, or solar panels. A sketch of two rows of the front array is shown in Figure 1. The aft, orthogonal set of mirrors would be placed directly behind the first, and would have varying depths in the orthogonal direction. Figures 2 and 3 show the complete fore and aft arrays respectively. The combined full array is shown in Figure 4.

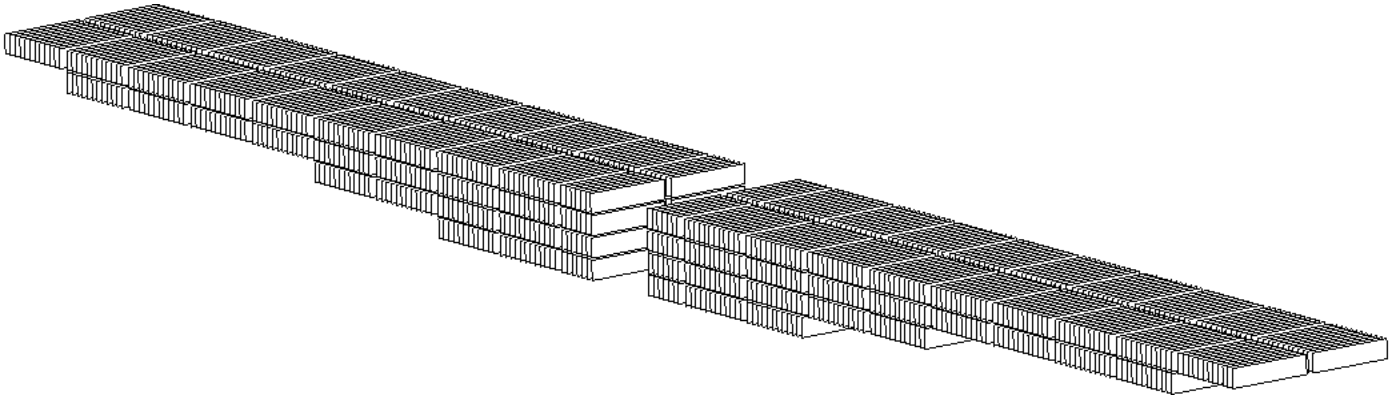

Figure 1

Alignment of the mirrors is dependent on the material used. A stretched membrane might rely on precision spacers and tensioning frames to position the mirrors, while a stiff lightweight material like Silicon Carbide or Zerodur may have alignment adjusters which can be bonded in place during the alignment process.

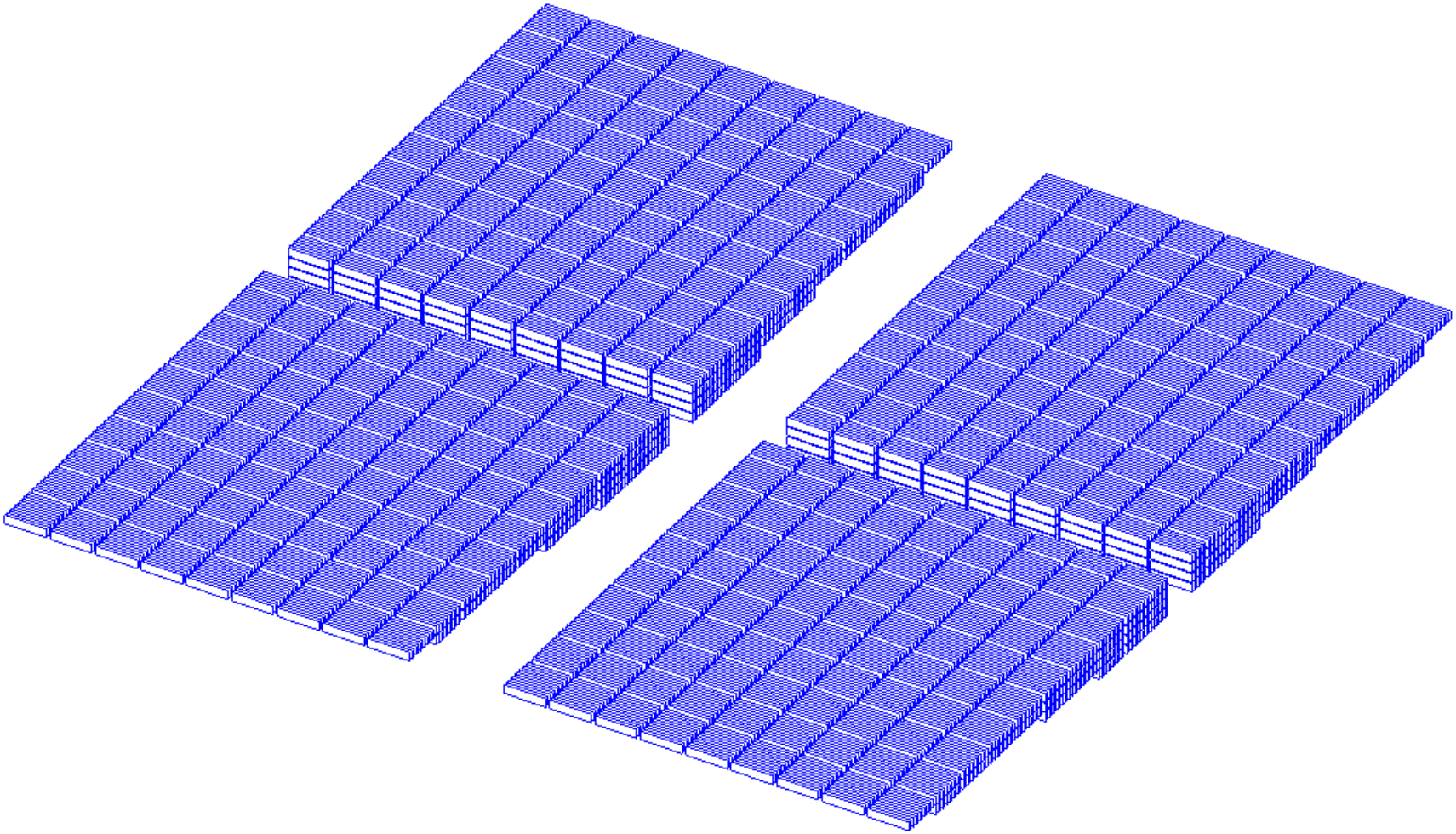

Figure 2 – Fore Array

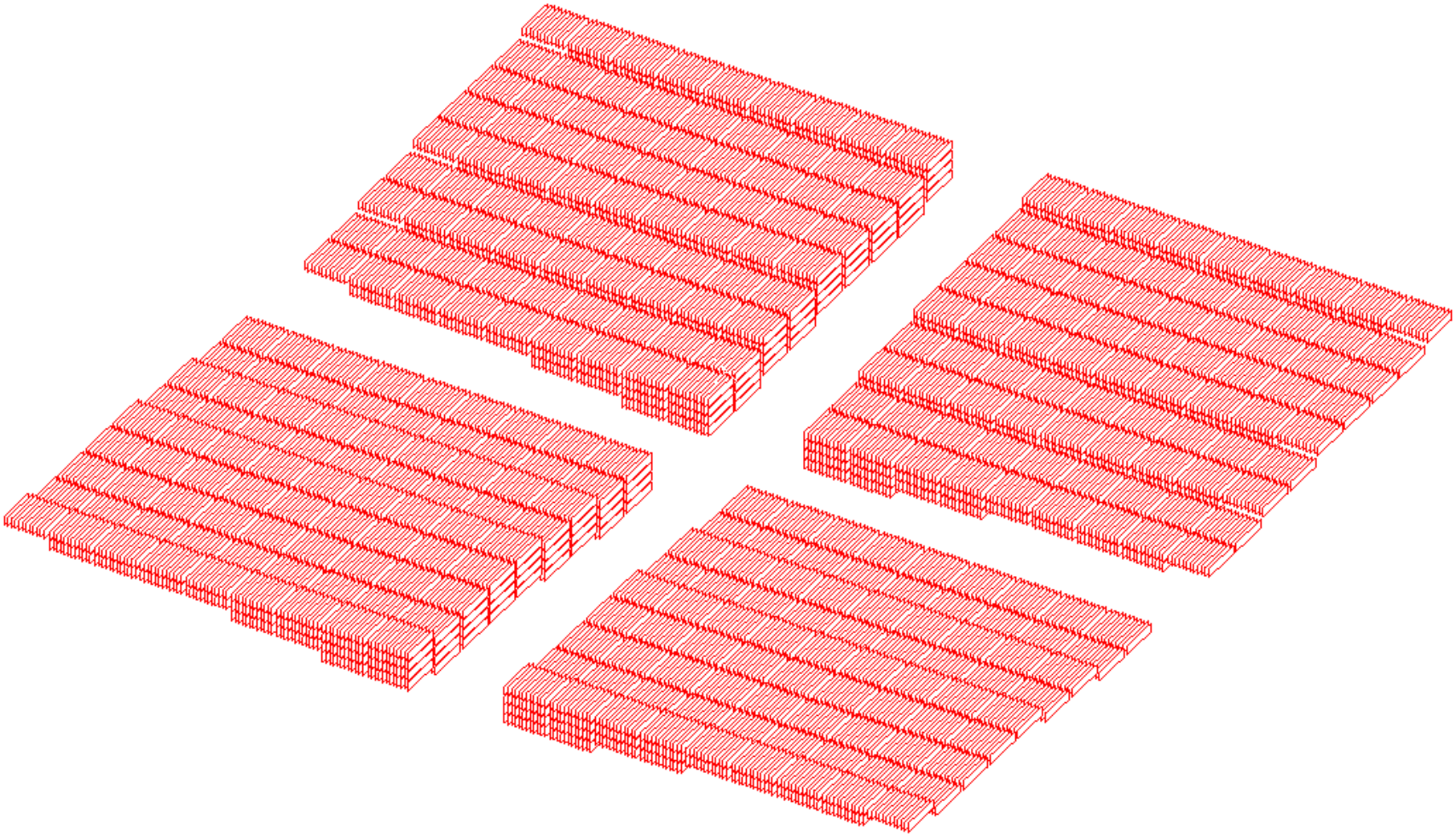

Figure 3 – Aft Array

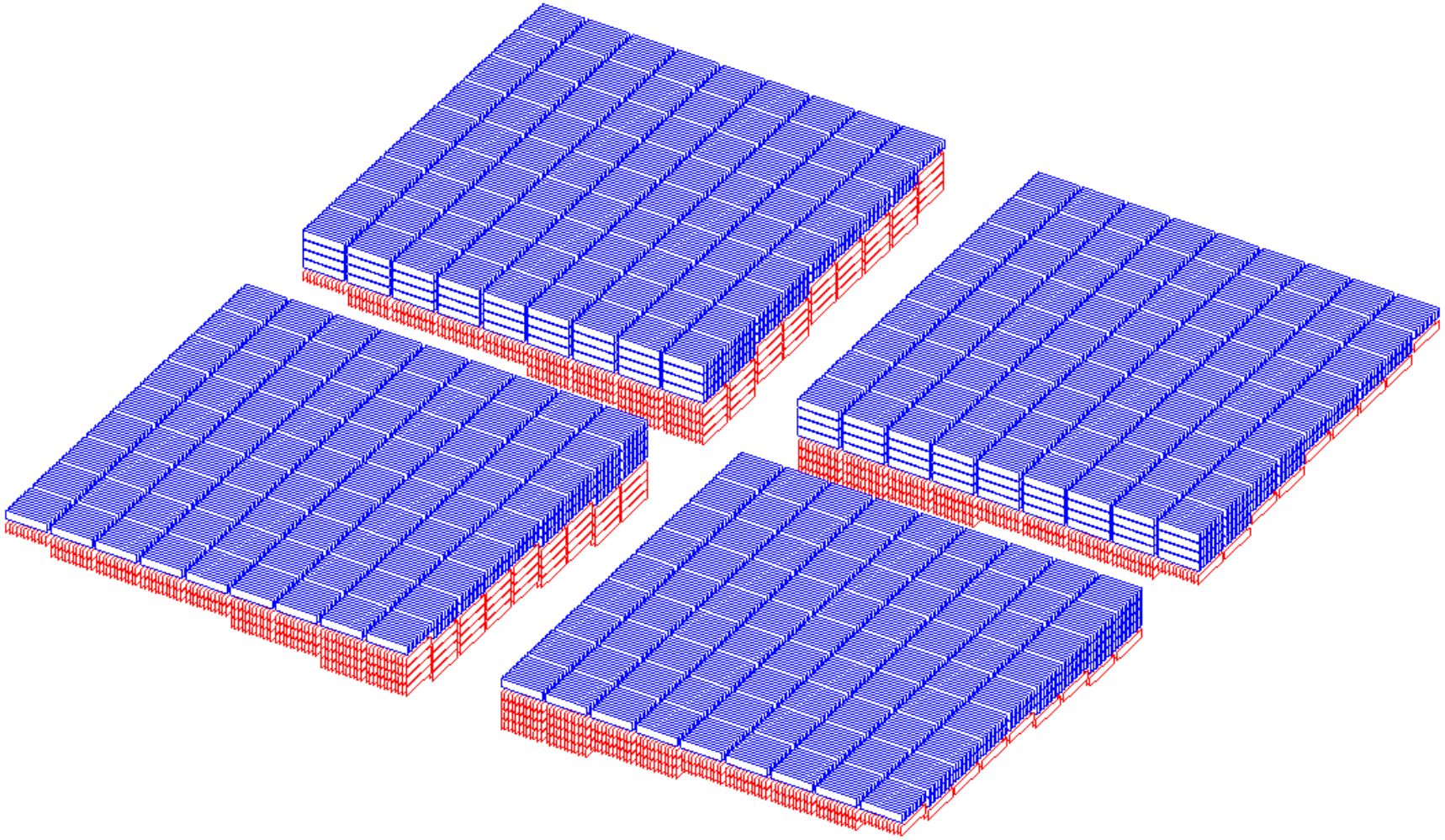

Figure 4 – Full Array

Appendix C
Finite Element Analysis of a polyester membrane subjected to uni-axial tension

Introduction:

The purpose of this analysis is to determine the extent to which a thin membrane with some degree of out-of-flat shape can be flattened by uni-axial tension. It is desirable to provide tension in only one direction, since frames which border the rectangular segments on all four sides would produce significant obscuration, given the tight spacing of the mirrors.

Discussion:

A finite element model of a 10cm x 50cm Mylar sheet is utilized to evaluate the figure change at a function of applied tension force. The initial shape is assumed to have a sinusoidal varying out-of-plane shape. Four cases of variation in the long direction are considered, from 0.5 cycles to 3 cycles across the length. Magnitudes of .001" .002" and .003" are modeled. The case of 0.5 cycles across the narrow direction is also modeled for the same three magnitude levels.

The Mylar membrane is modeled as .004" thick plate elements, with an elastic modulus of 550,000 psi. The model is shown in Figure 1.

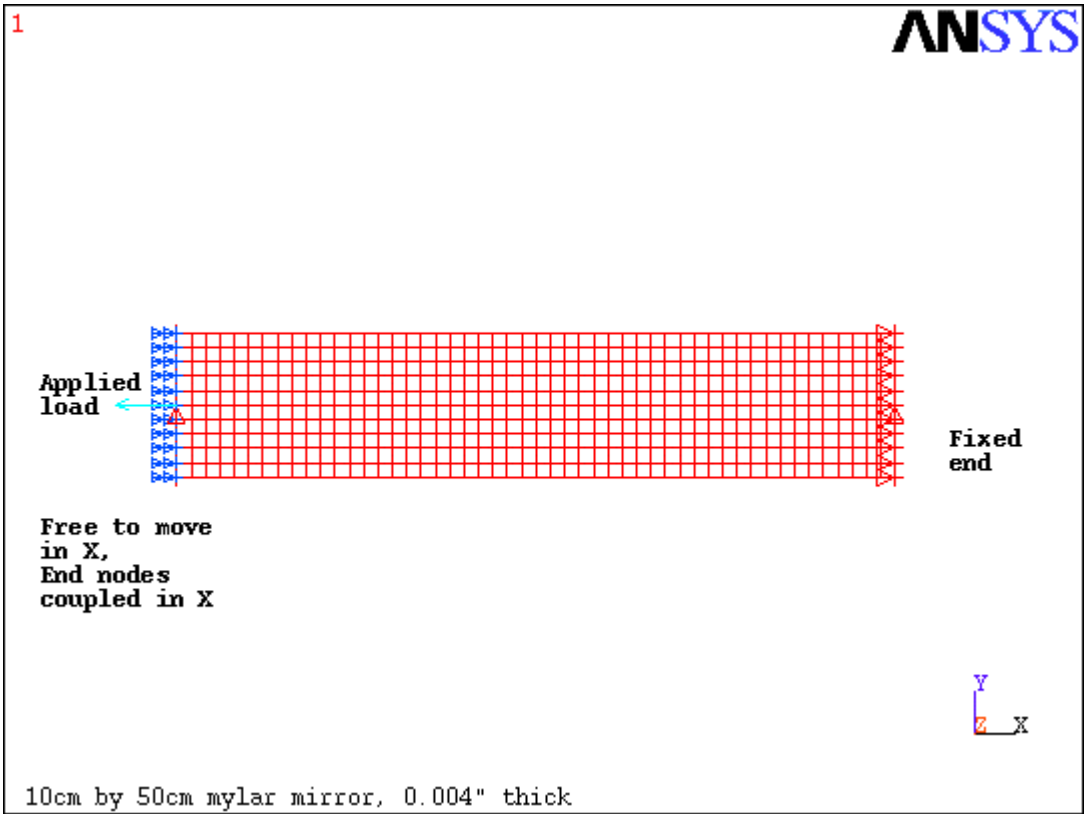

Figure 1 – ANSYS Finite Element Model

The undeformed shape error is accomplished by adjusting the "Z" coordinates of the for each case, to provide the initial stress free shape for that case. The boundary conditions at the narrow

edges include Z displacements on both ends to deflect the edge nodes to the desired plane, X restraints on the fixed end, and Y restraints at the center nodes on each end. The tensile load is applied to the left end of the model, in the long direction of the mirror. A non-linear analysis is performed with the ANSYS for each case for a range of loads, and the resulting deflections compared to the initial unstressed shape.

Results:

The maximum out-of-plane deformations due to tensile loads for all cases analyzed are presented in Tables 1 through 5. Deflection vs. load plots for each family of shapes and load ranges are included in Figures 2 through 6.

Representative contour plots are included in Figures 7 through 11. Examination of the results indicates that figure variations in the tension direction are much more easily flattened than those in the short direction. Figure 12 is a graph containing approximate residual deformations as a fraction of the original errors. This is calculated for each case by the equation:

$$Resid = \left|(UZ_{max} - FigErr)/FigErr\right|$$

Where: Resid = approximate residual error

UZ_{max} = maximum absolute displacement

FigErr = magnitude of original shape

This is approximate because it doesn't combine the deformations with the original shape on a node for node basis. This will be done in subsequent analyses. Figure 12 shows "kinks" in the curves for the long direction sine cases, due to some curling of the edges, which gets corrected as tension increases. It also shows that considerably more force is necessary to flatten the mirror in the transverse direction. For example, the half sine in the long direction is attenuated to $1/100^{th}$ of the original error with ~.02 lbs, the three sine in the long direction requires ~3 lbs., but the half sine in the short direction needs 30 lbs for the same attenuation.

Conclusions:

It can be seen from the results, that it is possible to flatten the mirror when the curvature is in the short direction, however it takes considerably more tension to flatten the mirror than the long direction. This material has several advantages of light weight, high resilience, and low obscuration. There are a number of challenges to meet in order to make this a viable material option. Measurement of the surfaces under the influence of gravity, co-alignment of the mirrors with each other, and design of tensioning and assembly techniques must be developed. Also, experimentation to verify this and additional analyses and construction of breadboard mirror assemblies will be necessary.

Table 1 – Half Sine Cycle in Long Direction

Applied Load	0.5sin-.001"	0.5sin-.002"	0.5sin-.003"
(lbs)	Max deflection (inches)		
0.0003	5.060E-04	1.013E-03	1.518E-03
0.0005	6.322E-04	1.264E-03	1.896E-03
0.001	7.772E-04	1.554E-03	2.332E-03
0.003	9.177E-04	1.835E-03	2.753E-03
0.005	9.522E-04	1.904E-03	2.856E-03
0.008	9.727E-04	1.945E-03	2.918E-03
0.01	9.797E-04	1.960E-03	2.939E-03
0.015	9.893E-04	1.978E-03	2.967E-03
0.02	9.944E-04	1.988E-03	2.982E-03
0.03	9.988E-04	1.998E-03	2.996E-03
0.04	1.001E-03	2.002E-03	3.025E-03
0.05	1.003E-03	2.005E-03	3.025E-03
0.06	1.004E-03	2.007E-03	3.025E-03
0.07	1.004E-03	2.017E-03	3.025E-03
0.08	1.005E-03	2.017E-03	3.016E-03
0.09	1.005E-03	2.017E-03	3.018E-03
0.1	1.005E-03	2.016E-03	3.019E-03
0.2	1.008E-03	2.013E-03	3.019E-03
0.3	1.006E-03	2.011E-03	3.020E-03
0.4	1.006E-03	2.012E-03	3.018E-03
0.5	1.006E-03	2.012E-03	3.018E-03
0.6	1.006E-03	2.012E-03	3.017E-03
0.7	1.006E-03	2.011E-03	3.017E-03
0.8	1.005E-03	2.010E-03	3.016E-03
0.9	1.005E-03	2.010E-03	3.015E-03
1	1.005E-03	2.010E-03	3.014E-03
2	1.004E-03	2.007E-03	3.011E-03
3	1.003E-03	2.006E-03	3.009E-03
4	1.003E-03	2.005E-03	3.008E-03
5	1.002E-03	2.005E-03	3.007E-03

Table 2 – One Sine Cycle in Long Direction

Applied Load	1sin-.001"	1sin-.002"	1sin-.003"
(lbs)	Max deflection (inches)		
0.0003	2.049E-04	4.097E-04	6.143E-04
0.0005	3.014E-04	6.028E-04	9.040E-04
0.001	4.662E-04	9.324E-04	1.398E-03
0.003	7.334E-04	1.467E-03	2.200E-03
0.005	8.282E-04	1.657E-03	2.485E-03
0.008	8.931E-04	1.786E-03	2.680E-03
0.01	9.170E-04	1.834E-03	2.751E-03
0.015	9.508E-04	1.902E-03	2.852E-03
0.02	9.686E-04	1.937E-03	2.906E-03
0.03	9.866E-04	1.973E-03	2.960E-03
0.04	9.956E-04	1.991E-03	2.987E-03
0.05	1.001E-03	2.002E-03	3.003E-03
0.06	1.004E-03	2.008E-03	3.013E-03
0.07	1.007E-03	2.013E-03	3.020E-03
0.08	1.008E-03	2.016E-03	3.024E-03
0.09	1.009E-03	2.021E-03	3.033E-03
0.1	1.010E-03	2.020E-03	3.035E-03
0.2	1.013E-03	2.024E-03	3.034E-03
0.3	1.015E-03	2.026E-03	3.035E-03
0.4	1.012E-03	2.025E-03	3.032E-03
0.5	1.010E-03	2.019E-03	3.029E-03
0.6	1.009E-03	2.019E-03	3.028E-03
0.7	1.009E-03	2.018E-03	3.025E-03
0.8	1.008E-03	2.017E-03	3.024E-03
0.9	1.008E-03	2.016E-03	3.022E-03
1	1.007E-03	2.014E-03	3.021E-03
2	1.005E-03	2.009E-03	3.013E-03
3	1.003E-03	2.007E-03	3.010E-03
4	1.003E-03	2.005E-03	3.008E-03
5	1.002E-03	2.005E-03	3.007E-03

Table 3 – Two Sine Cycles in Long Direction

Applied Load	2sin-.001"	2sin-.002"	2sin-.003"
(lbs)	Max deflection (inches)		
0.0003	6.131E-05	1.222E-04	1.824E-04
0.0005	9.842E-05	1.963E-04	2.931E-04
0.001	1.803E-04	3.597E-04	5.376E-04
0.003	4.046E-04	8.082E-04	1.210E-03
0.005	5.384E-04	1.076E-03	1.613E-03
0.008	6.611E-04	1.322E-03	1.982E-03
0.01	7.153E-04	1.430E-03	2.145E-03
0.015	8.026E-04	1.605E-03	2.407E-03
0.02	8.543E-04	1.709E-03	2.563E-03
0.03	9.120E-04	1.824E-03	2.736E-03
0.04	9.430E-04	1.886E-03	2.829E-03
0.05	9.620E-04	1.924E-03	2.886E-03
0.06	9.747E-04	1.949E-03	2.923E-03
0.07	9.832E-04	1.966E-03	2.950E-03
0.08	9.896E-04	1.979E-03	2.969E-03
0.09	9.944E-04	1.989E-03	2.983E-03
0.1	9.981E-04	1.996E-03	2.994E-03
0.2	1.012E-03	2.023E-03	3.035E-03
0.3	1.014E-03	2.035E-03	3.045E-03
0.4	1.015E-03	2.028E-03	3.043E-03
0.5	1.015E-03	2.026E-03	3.042E-03
0.6	1.015E-03	2.025E-03	3.041E-03
0.7	1.015E-03	2.025E-03	3.039E-03
0.8	1.019E-03	2.024E-03	3.037E-03
0.9	1.030E-03	2.023E-03	3.036E-03
1	1.012E-03	2.023E-03	3.035E-03
2	1.011E-03	2.018E-03	3.027E-03
3	1.008E-03	2.015E-03	3.023E-03
4	1.006E-03	2.013E-03	3.020E-03
5	1.006E-03	2.012E-03	3.017E-03

Table 4 – Three Sine Cycles in Long Direction

Applied Load	3sin-.001"	3sin-.002"	3sin-.003"
(lbs)	Max deflection (inches)		
0.0003	2.820E-05	5.590E-05	8.297E-05
0.0005	4.620E-05	9.160E-05	1.360E-04
0.001	8.860E-05	1.760E-04	2.614E-04
0.003	2.290E-04	4.550E-04	6.777E-04
0.005	3.340E-04	6.660E-04	9.939E-04
0.008	4.520E-04	9.010E-04	1.346E-03
0.01	5.110E-04	1.020E-03	1.526E-03
0.015	6.200E-04	1.238E-03	1.855E-03
0.02	6.930E-04	1.386E-03	2.076E-03
0.03	7.850E-04	1.570E-03	2.354E-03
0.04	8.400E-04	1.680E-03	2.520E-03
0.05	8.760E-04	1.752E-03	2.628E-03
0.06	9.010E-04	1.803E-03	2.704E-03
0.07	9.200E-04	1.840E-03	2.760E-03
0.08	9.340E-04	1.868E-03	2.803E-03
0.09	9.450E-04	1.890E-03	2.836E-03
0.1	9.540E-04	1.908E-03	2.863E-03
0.2	9.920E-04	1.985E-03	2.978E-03
0.3	1.003E-03	2.007E-03	3.011E-03
0.4	1.008E-03	2.016E-03	3.025E-03
0.5	1.010E-03	2.021E-03	3.031E-03
0.6	1.012E-03	2.024E-03	3.040E-03
0.7	1.012E-03	2.026E-03	3.037E-03
0.8	1.013E-03	2.025E-03	3.041E-03
0.9	1.013E-03	2.025E-03	3.041E-03
1	1.013E-03	2.026E-03	3.041E-03
2	1.012E-03	2.023E-03	3.033E-03
3	1.010E-03	2.020E-03	3.031E-03
4	1.009E-03	2.019E-03	3.028E-03
5	1.008E-03	2.017E-03	3.025E-03

Table 5 – Half Sine Cycle in Short Direction

Force	.5 cycle in narrow direction
(lbs)	Max defl. in.
0.0002	4.844E-04
0.0003	5.146E-04
0.0005	5.517E-04
0.001	5.910E-04
0.003	6.243E-04
0.005	6.292E-04
0.008	6.313E-04
0.01	6.318E-04
0.015	6.327E-04
0.02	6.332E-04
0.03	6.343E-04
0.04	6.354E-04
0.05	6.366E-04
0.06	6.379E-04
0.07	6.393E-04
0.08	6.408E-04
0.09	6.423E-04
0.1	6.438E-04
0.2	6.614E-04
0.3	6.798E-04
0.4	6.974E-04
0.5	7.138E-04
0.6	7.289E-04
0.7	7.427E-04
0.8	7.553E-04
0.9	7.669E-04
1	7.775E-04
2	8.489E-04
3	8.869E-04
4	9.104E-04
5	9.264E-04
8	9.532E-04
10	9.630E-04
20	9.834E-04
30	9.901E-04
40	9.932E-04
50	9.949E-04
80	9.972E-04
100	9.978E-04

Figure 2

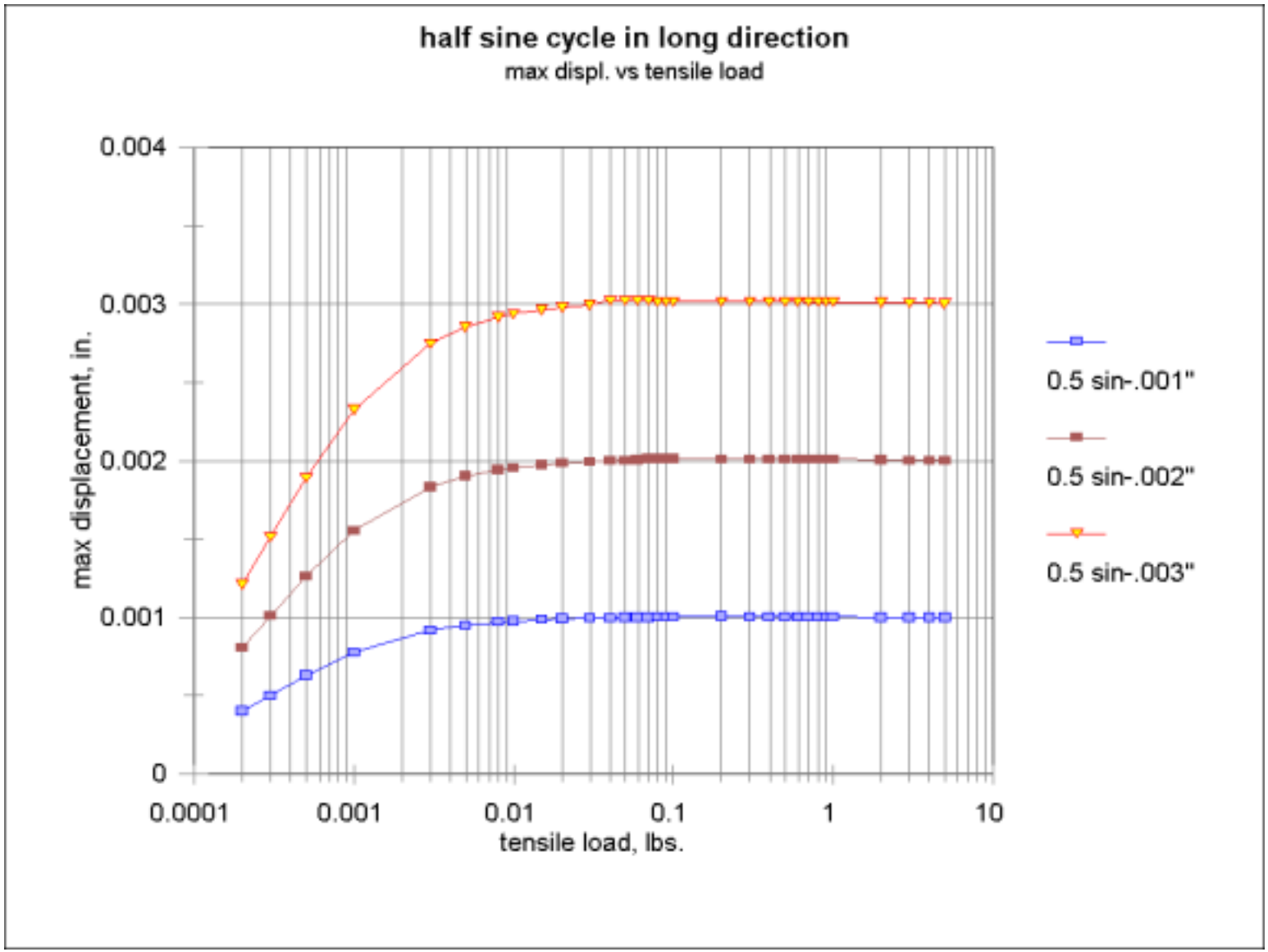
half sine cycle in long direction
max displ. vs tensile load
max displacement, in.
0.004
0.003
0.002
0.001
0
0.0001
0.001
0.01
0.1
1
10
tensile load, lbs.
0.5 sin-.001"
0.5 sin-.002"
0.5 sin-.003"

Figure 3

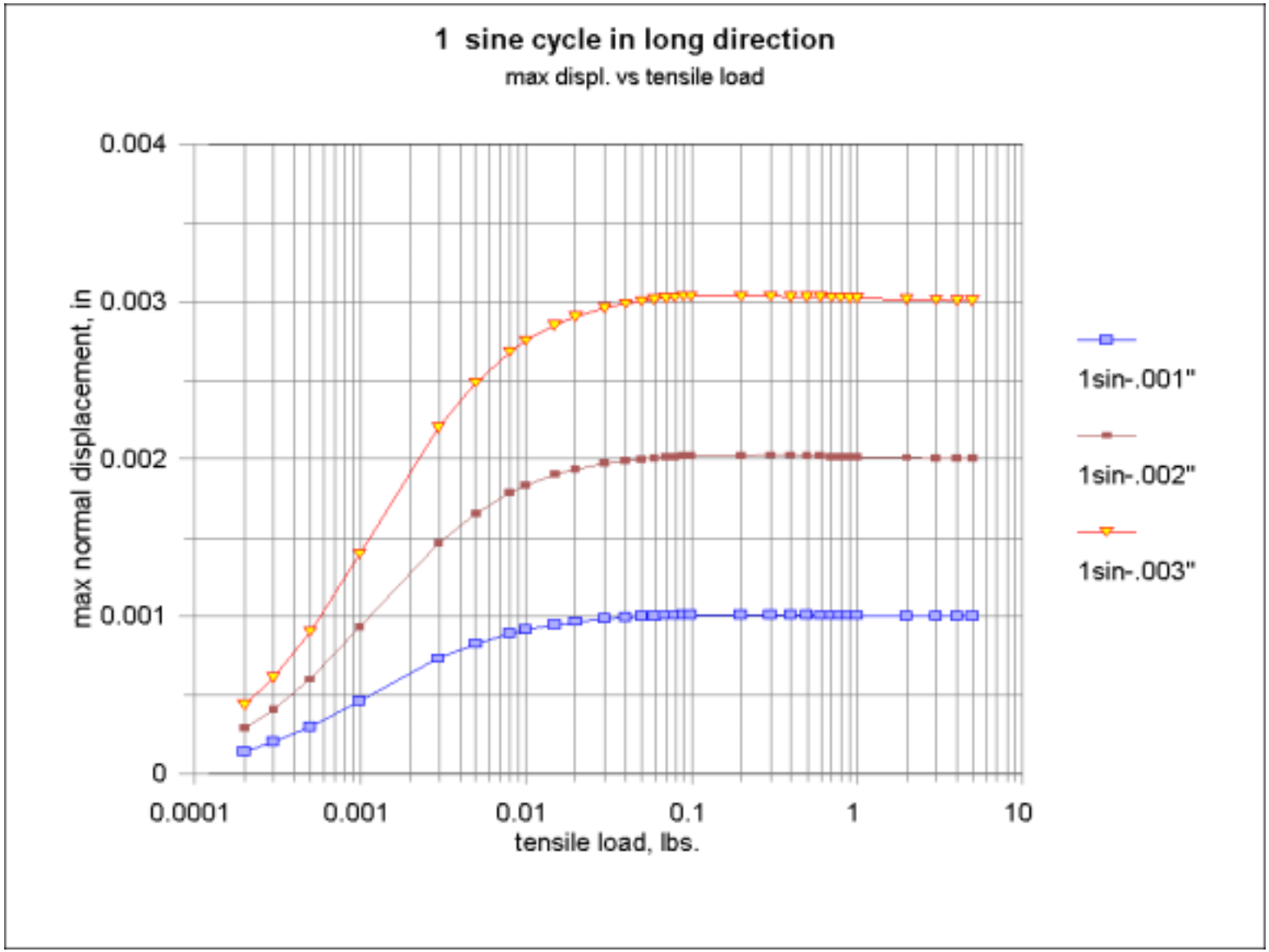
1 sine cycle in long direction
max displ. vs tensile load
max normal displacement, in
0.004
0.003
0.002
0.001
0
0.0001
0.001
0.01
0.1
1
10
tensile load, lbs.
1sin-.001"
1sin-.002"
1sin-.003"

Figure 4

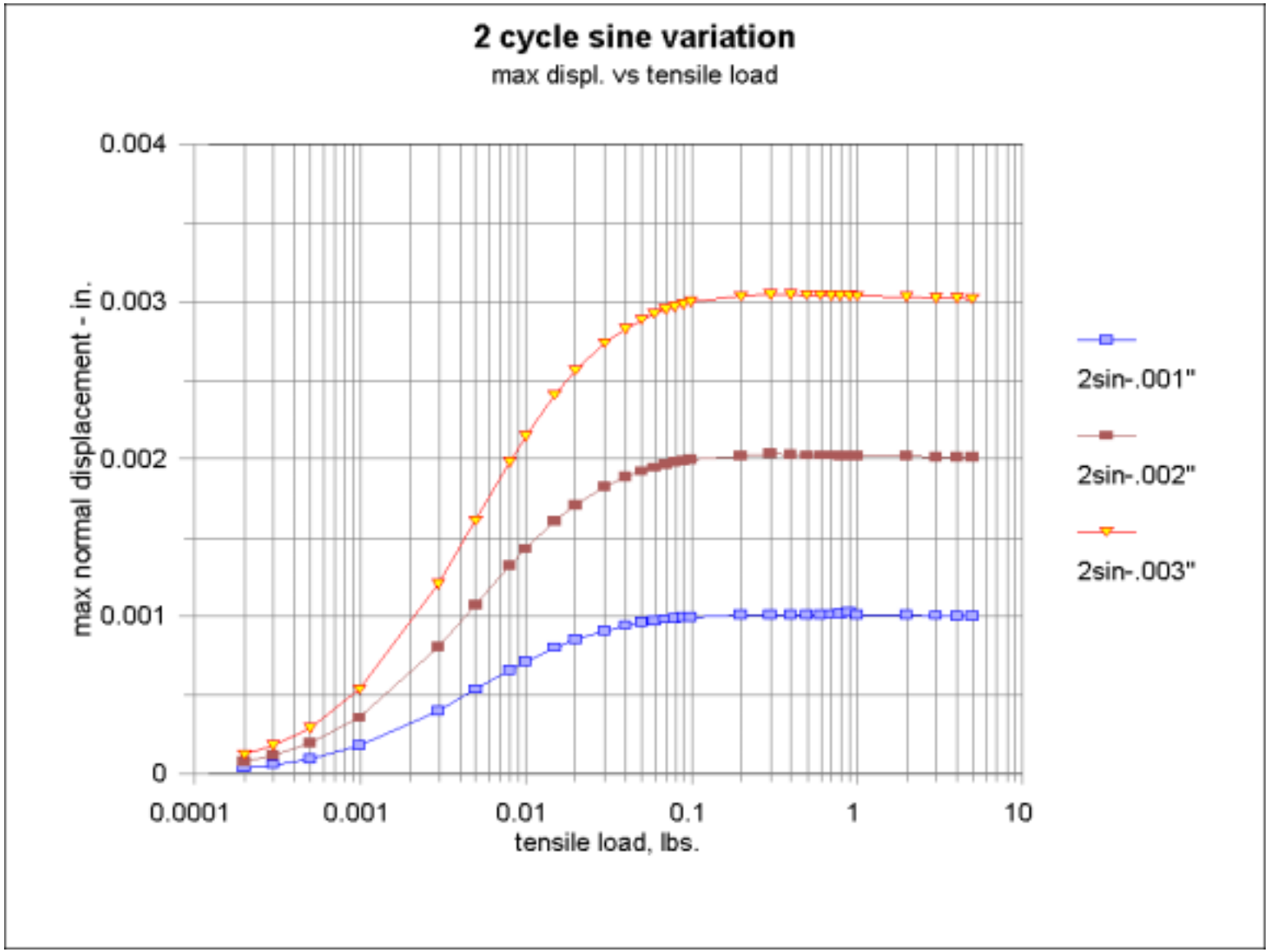
2 cycle sine variation
max displ. vs tensile load
max normal displacement - in.
0.004
0.003
0.002
0.001
0
0.0001
0.001
0.01
0.1
1
10
tensile load, lbs.
2sin-.001"
2sin-.002"
2sin-.003"

Figure 5

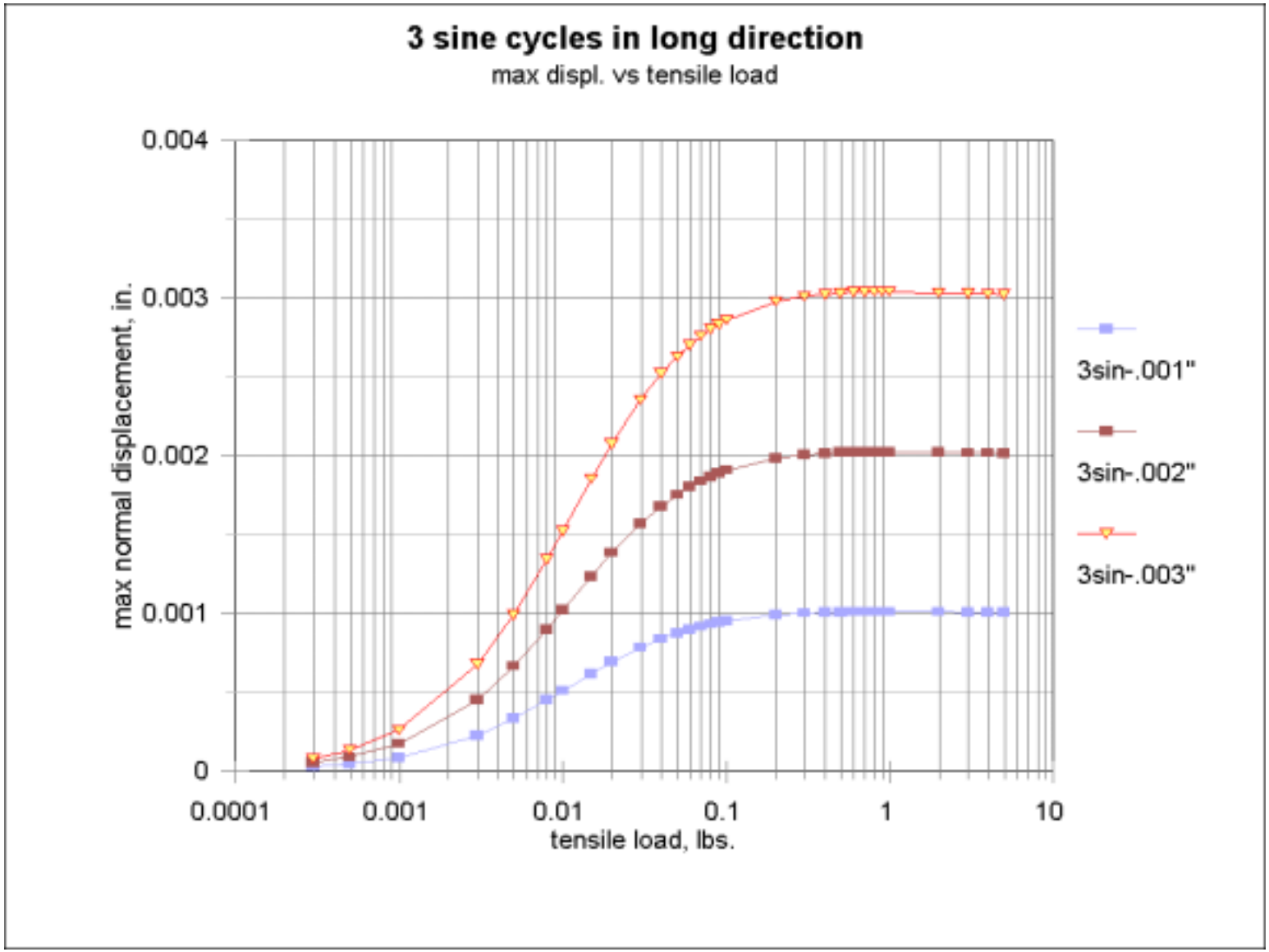
3 sine cycles in long direction
max displ. vs tensile load
max normal displacement, in.
0.004
0.003
0.002
0.001
0
0.0001
0.001
0.01
0.1
1
10
tensile load, lbs.
3sin-.001"
3sin-.002"
3sin-.003"

Figure 6

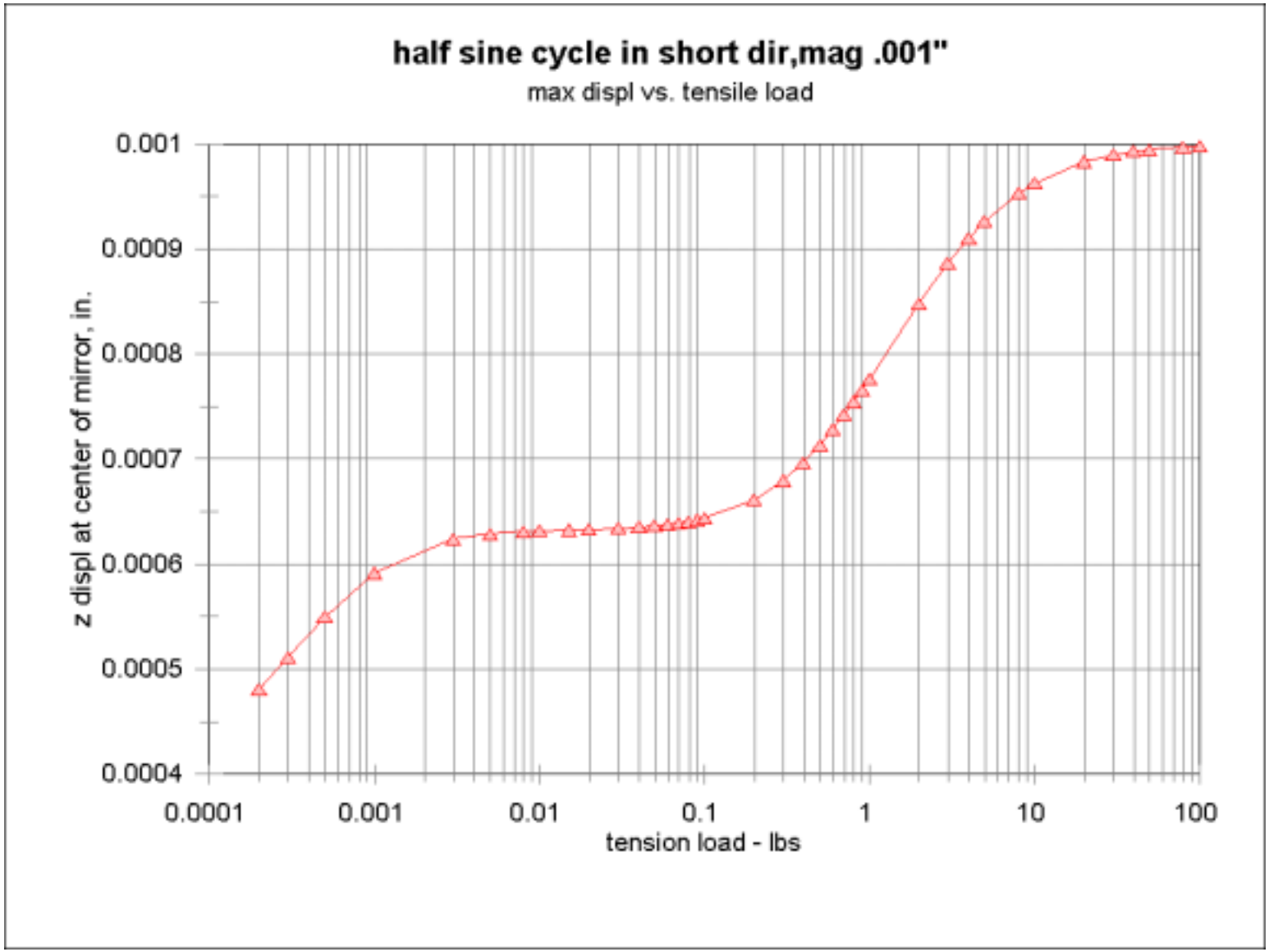
half sine cycle in short dir,mag .001"
max displ vs. tensile load
z displ at center of mirror, in.
0.001
0.0009
0.0008
0.0007
0.0006
0.0005
0.0004
0.0001
0.001
0.01
0.1
1
10
100
tension load - lbs

Figure 7

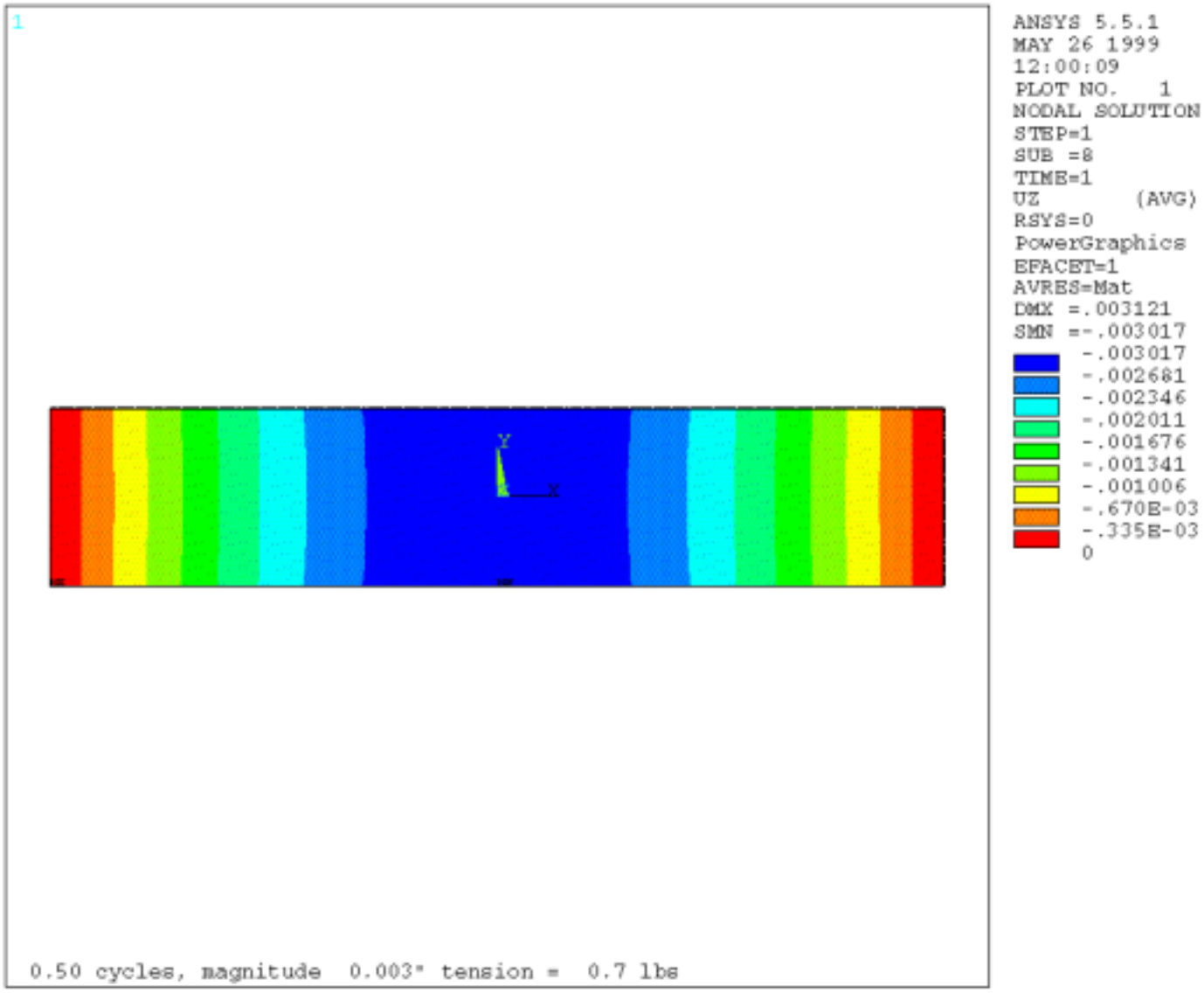
1
ANSYS 5.5.1
MAY 26 1999
12:00:09
PLOT NO. 1
NODAL SOLUTION
STEP=1
SUB =8
TIME=1
UZ (AVG)
RSYS=0
PowerGraphics
EFACET=1
AVRES=Mat
DMX =.003121
SMN =-.003017
-.003017
-.002681
-.002346
-.002011
-.001676
-.001341
-.001006
-.670E-03
-.335E-03
0
0.50 cycles, magnitude 0.003" tension = 0.7 lbs

Figure 8

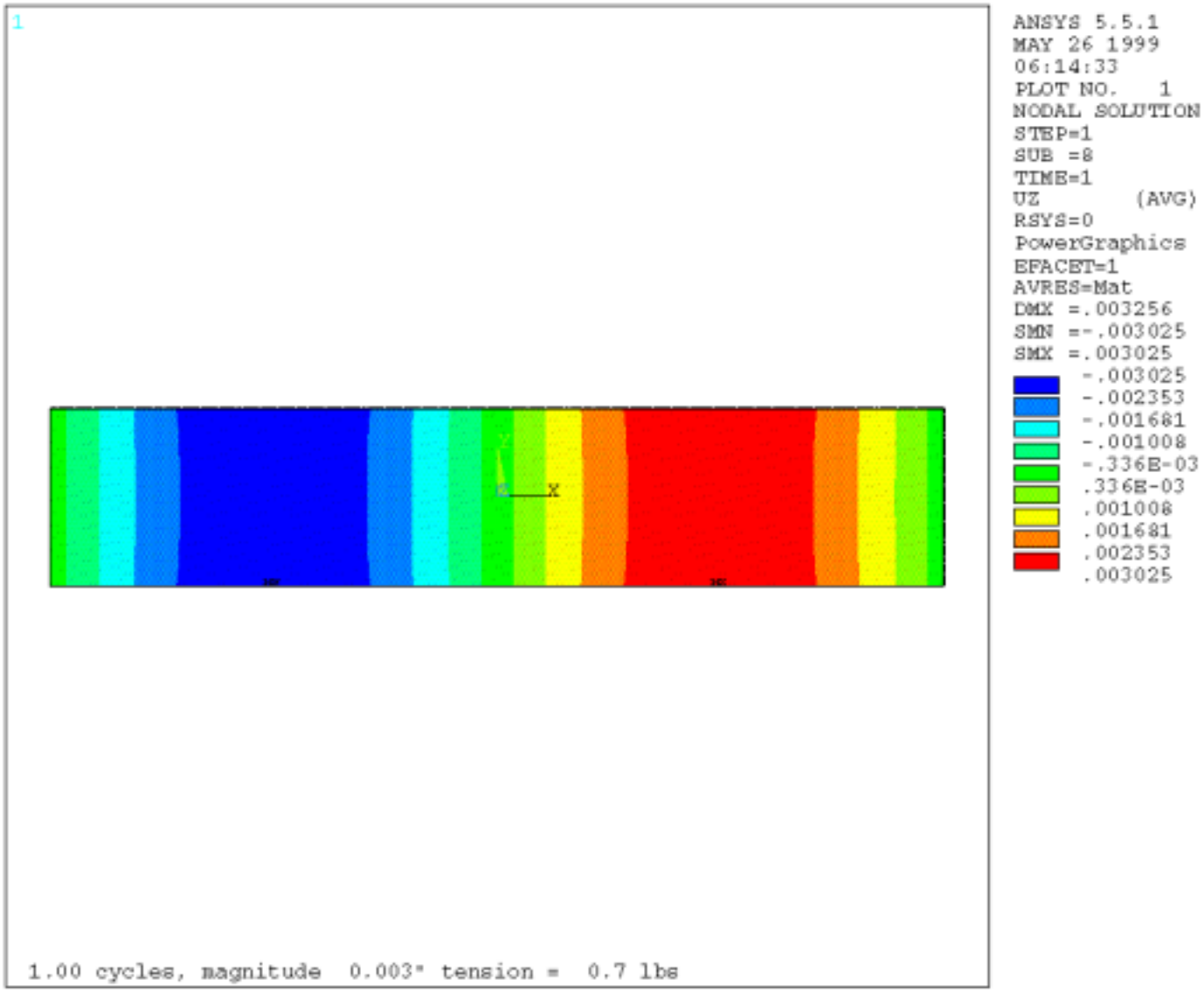
1
ANSYS 5.5.1
MAY 26 1999
06:14:33
PLOT NO. 1
NODAL SOLUTION
STEP=1
SUB =8
TIME=1
UZ (AVG)
RSYS=0
PowerGraphics
EFACET=1
AVRES=Mat
DMX =.003256
SMN =-.003025
SMX =.003025
-.003025
-.002353
-.001681
-.001008
-.336E-03
.336E-03
.001008
.001681
.002353
.003025
1.00 cycles, magnitude 0.003" tension = 0.7 lbs

Figure 9

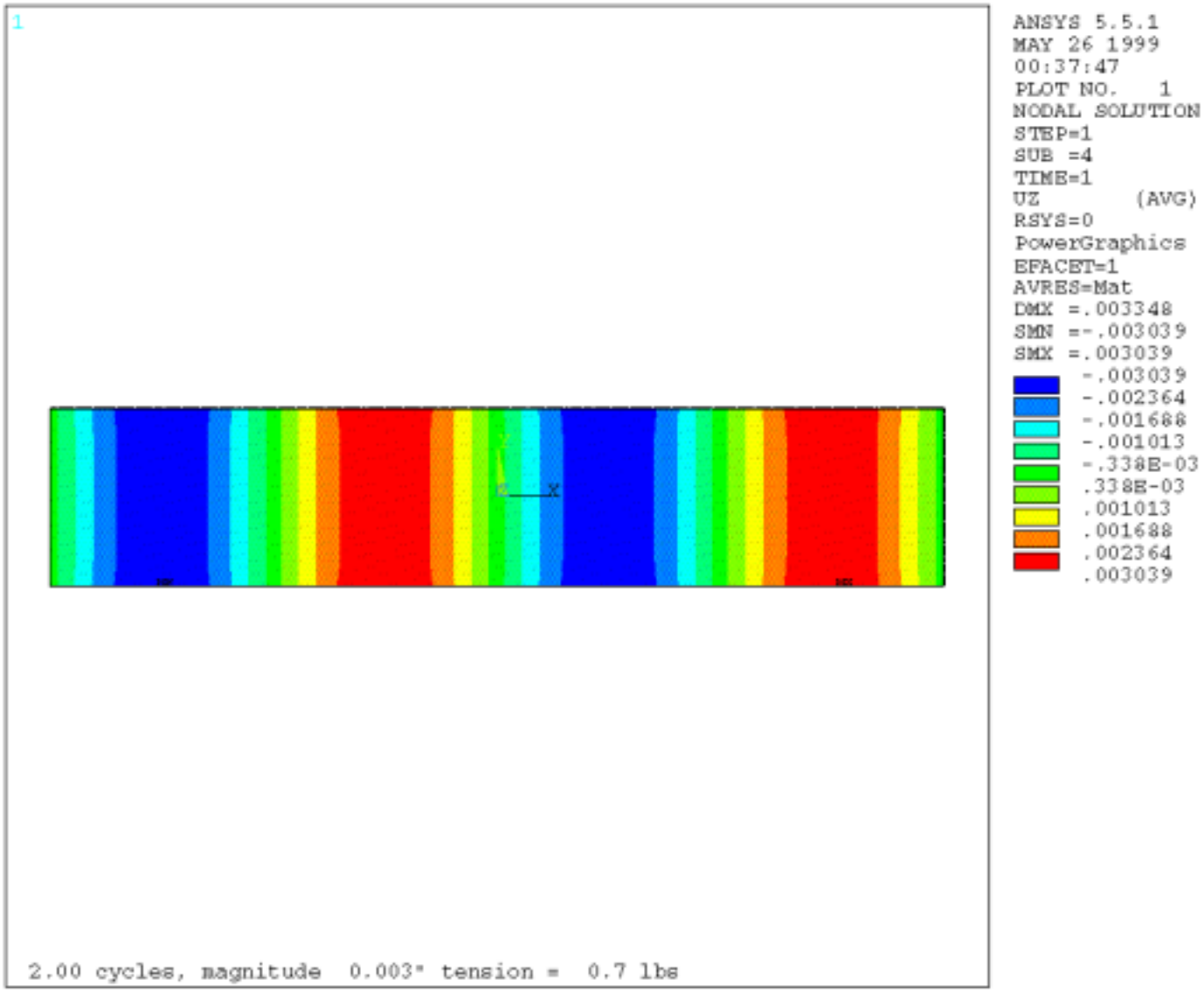
1
ANSYS 5.5.1
MAY 26 1999
00:37:47
PLOT NO. 1
NODAL SOLUTION
STEP=1
SUB =4
TIME=1
UZ (AVG)
RSYS=0
PowerGraphics
EFACET=1
AVRES=Mat
DMX =.003348
SMN =-.003039
SMX =.003039
-.003039
-.002364
-.001688
-.001013
-.338E-03
.338E-03
.001013
.001688
.002364
.003039
2.00 cycles, magnitude 0.003" tension = 0.7 lbs

Figure 10

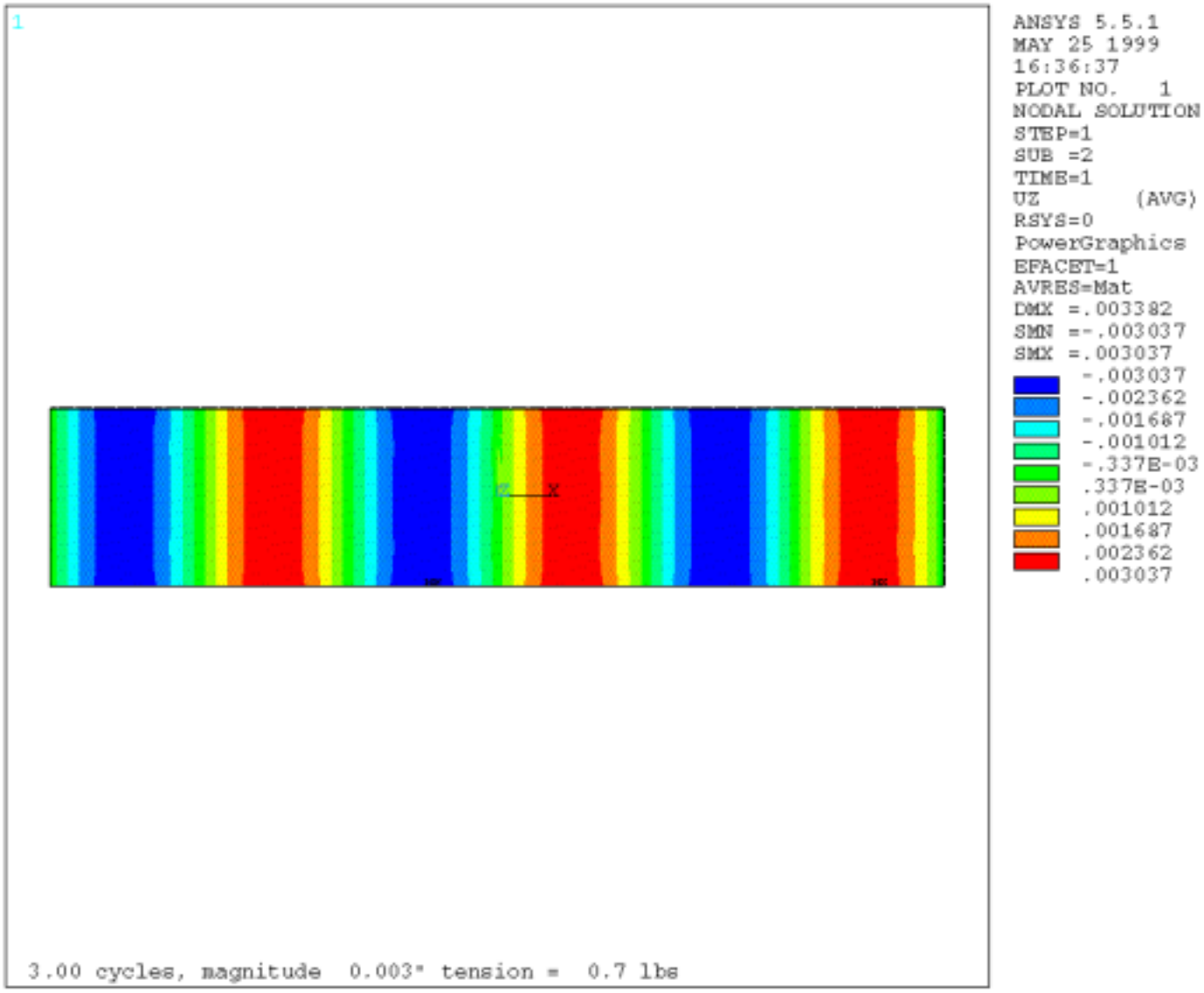
1
ANSYS 5.5.1
MAY 25 1999
16:36:37
PLOT NO. 1
NODAL SOLUTION
STEP=1
SUB =2
TIME=1
UZ (AVG)
RSYS=0
PowerGraphics
EFACET=1
AVRES=Mat
DMX =.003382
SMN =-.003037
SMX =.003037
-.003037
-.002362
-.001687
-.001012
-.337E-03
.337E-03
.001012
.001687
.002362
.003037
3.00 cycles, magnitude 0.003" tension = 0.7 lbs

Figure 11

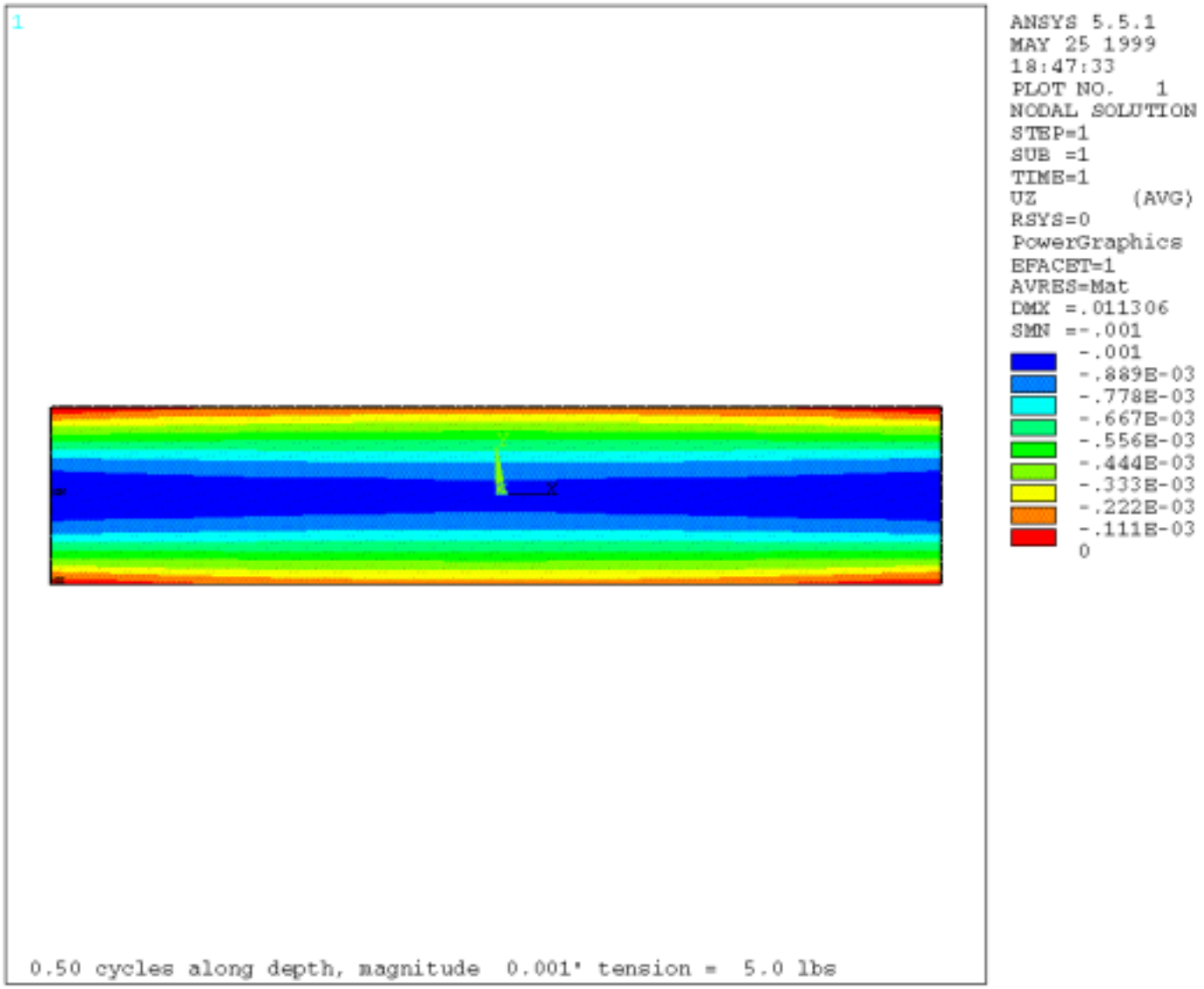
1
ANSYS 5.5.1
MAY 25 1999
18:47:33
PLOT NO. 1
NODAL SOLUTION
STEP=1
SUB =1
TIME=1
UZ (AVG)
RSYS=0
PowerGraphics
EFACET=1
AVRES=Mat
DMX =.011306
SMN =-.001
-.001
-.889E-03
-.778E-03
-.667E-03
-.556E-03
-.444E-03
-.333E-03
-.222E-03
-.111E-03
0
0.50 cycles along depth, magnitude 0.001" tension = 5.0 lbs

Figure 12

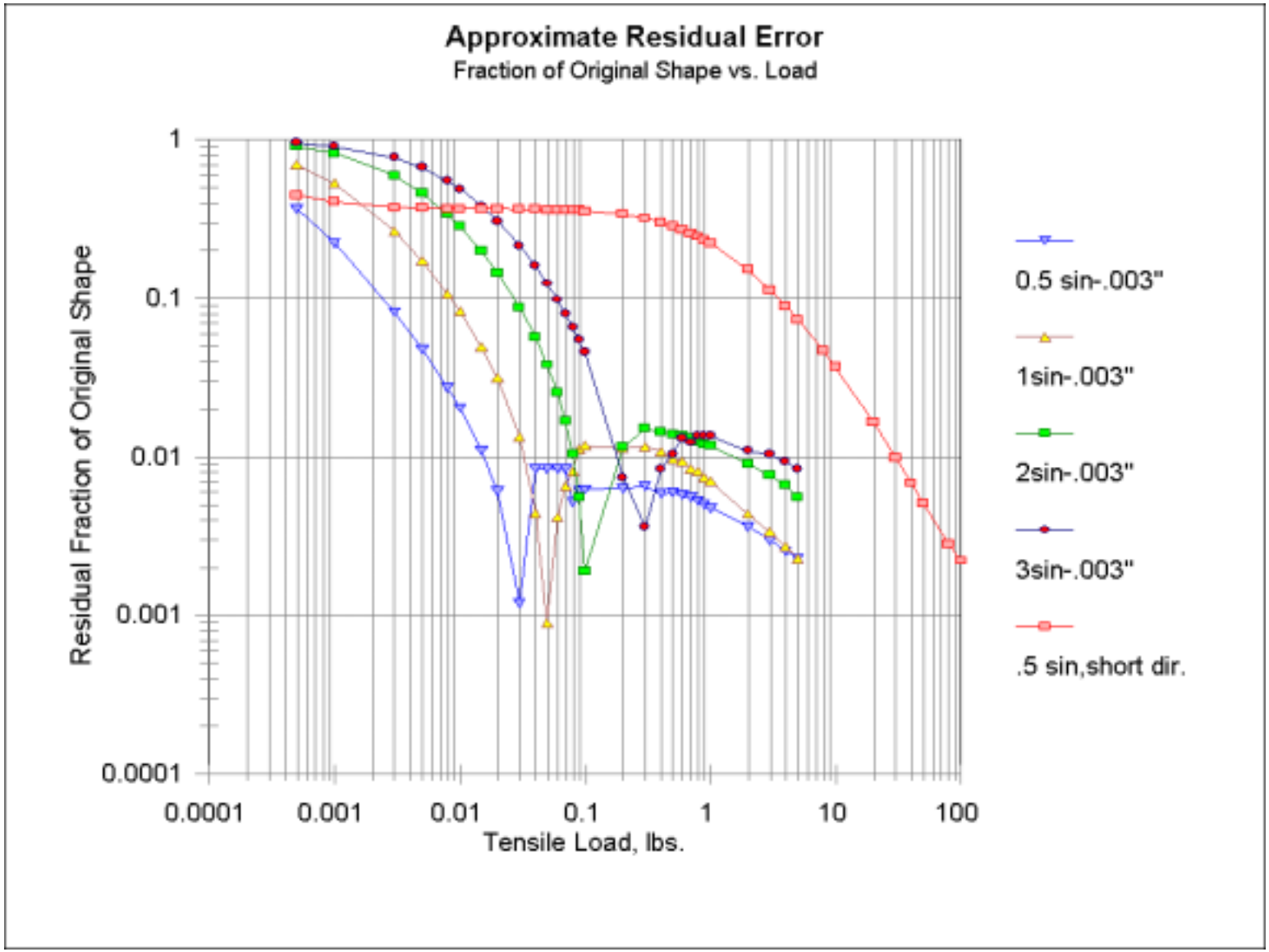
Approximate Residual Error
Fraction of Original Shape vs. Load
Residual Fraction of Original Shape
1
0.1
0.01
0.001
0.0001
0.0001
0.001
0.01
0.1
1
10
100
Tensile Load, lbs.
0.5 sin-.003"
1sin-.003"
2sin-.003"
3sin-.003"
.5 sin,short dir.

References

Baudaz, M., Peacock, A., Parmer, A., Beijersbergen, M., and Schiemann, J., 1999 ESLAB1999/003/SA (To be published in 2nd European Symposium on Utilization of the Space Station).

Blandino, J.J., et al, Pulsed Plasma Thrusters for the New Millennium Interferometer (DS-3) Mission, IEPC-97-192.

David, L.P., 1999 (Submittted to Ap. J.)

Cen, R., and Ostriker. J.P,, 1998, astro-ph/9806281

Cen, R., and Ostriker, J.P., 1999, Ap.J. **514**, 1.

Haag, T., Curran, F., High-Power Hydrogen Arcjet Performance AIAA-91-2226.

Hailey, C. J., Abdali, S., Christensen, F. E., Craig, W. W., Decker, T. R., Harrison, F. A. , Jiminez-Garate, M. A., 1997, SPIE 3114, 535.

Lichon, P., Sankovic, J., Development and Demonstration of a 600 Second Mission Average Arcjet, IEPC-93-087.

Lund, N., 1992, Experimental Astronomy bf 2, 259.

Munoz, J.A., Kochanek, C.S., and Falco, E.E.,1999 (Submitted to Ap.J. Letters) ASTRO-PH/9905293.

Myers, R.M., Electromagnetic Propulsion for Spacecraft, AIAA-93-1086.

Perna,R., and Loeb, A., 1998, Ap.J., **503**, L135.

Renzini, A., 1999, Astro-ph/9902361.

Sankovic, et al , The BMDO Russian Hall Electric Thruster Technology (RHETT) Program: From Laboratory to Orbit.

Shibata, R., et al, 1998 SPIE 3444, **598**.

Smither, R. K., 1984, US Patent No. bf 4,429, 411.

Soong, Y., Jalota, L., Serlemitsos, P., 1995, SPIE **2515**, 64.

Sovey ,J., et al, Development of an Jon Thruster and Power Processor for New Millennium Deep Space 1 Mission AIAA-97-2778.

Vogeley, M.S., 1998, Ap.J.

von Ballmoos, P., and Smither, R, K., 1994 Ap. J. Suppl. Ser., bf92, 663